國立臺灣大學電機資訊學院電信工程學研究所

博士論文

Graduate Institute of Communication Engineering
College of Electrical Engineering and Computer Science
National Taiwan University
Doctoral Dissertation

太陽磁暴期間由地磁場導引電流感應的地面電場模擬

Simulations of GIE induced by Field-Aligned Current during Magnetic Storm

張哲睿
Che-Jui Chang

指導教授：江簡富 博士
Advisor: Jean-Fu Kiang, Ph.D.

中華民國 114 年 2 月
February 2025

doi:10.6342/NTU202500706

Acknowledgement

I would like to express profound gratitude to my advisor, Professor Jean-Fu Kiang, for his guidance, patience and support throughout my PhD journey. I extend my appreciation to my dissertation readers, Professors Chun-Hsing Li, Jian-Jiun Ding, Hsiang-Chieh Lee and Yu-Hsiang Cheng for their valuable comments to improve the quality of this dissertation. I would like to thank the faculty in the Department of Electrical Engineering and the Graduate Institute of Communication Engineering, Nation Taiwan University for providing the necessary resources and support that made this research possible. Special thanks to Mr. Jons Huang, Rotary Club of Taipei Tatung and Scholarship of Chung Hwa Rotary Education Foundation for recommending and choosing me as a scholar of the Chung Hwa Rotary Educational Foundation. I wish to convey my deepest gratefulness to my friends, my church brothers and sisters and my family for their unwavering companionship, encouragement and support throughout this journey.

doi:10.6342/NTU202500706

摘要

太空天氣在磁層和電離層的日變化中起著重要作用，從而影響大氣層內及地表的人類活動。太陽風攜帶星際磁場驅動空間中的地磁場導引電流，進而在地球表面產生地磁感應電場和地磁感應電流。地磁感應電流可能會損壞電網中的變壓器和傳輸線、鐵路設備、通信電纜以及管道網絡。文獻中通常將地表的地磁感應電場起源簡化為面電流或線電流。在本研究中，將探討地球表面的地磁感應電場與磁暴期間地磁場導引電流之間的關係。通過磁流體力學模型模擬地球磁暴期間磁層對太陽風的響應，並將該響應作為邊界條件，進一步模擬電離層的響應。最後，應用時域有限差分法計算基於電離層響應推導出的電流源，並獲得地磁感應電場的時空分佈。本研究模擬了 2017 年 5 月磁暴、萬聖節磁暴以及卡靈頓事件三種情境下的地磁感應電場分佈，以評估太陽風暴可能帶來的災害。此外，模擬中還揭示了類似范艾倫輻射帶的現象。

doi:10.6342/NTU202500706

Abstract

Space weather plays an important role in the diurnal variation of magnetosphere and ionosphere, hence impacts the human activities in the atmosphere and on the ground. The solar wind accompanied by the interplanetary magnetic field (IMF) drives field-aligned currents (FACs) in space, which in turn drive geomagnetically induced electric field (GIE) and geomagnetically induced current (GIC) on the Earth surface. The GIC may damage transformers and transmission lines in power grids, railway equipment, communication cables and pipeline networks. The ground-level GIE was assumed to originate from some simplified current sheet or line current in the literature. In this work, the relationship between GIE on the Earth surface and the FACs during a magnetic storm will be studied. The magnetospheric response to the solar wind during geomagnetic storms is simulated by using an MHD model. The ionospheric response is then simulated by taking the magnetospheric response as the boundary conditions. Finally, an FDTD method is applied to compute the spatial and temporal distributions of GIE in terms of the current sources derived from the ionospheric response. The distributions of GIE are simulated in three scenarios of May 2017

doi:10.6342/NTU202500706

storm, Halloween storm and Carrington storm, respectively, to evaluate possible hazards of solar storms. In addition, phenomena akin to the Van Allen radiation belts are revealed in the simulations.

doi:10.6342/NTU202500706

Contents

doi:10.6342/NTU202500706

doi:10.6342/NTU202500706

List of Figures

doi:10.6342/NTU202500706

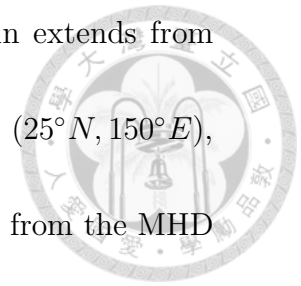

doi:10.6342/NTU202500706

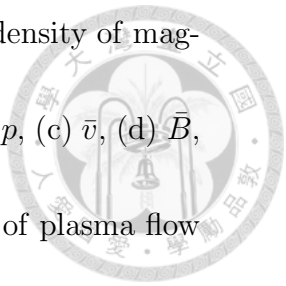

doi:10.6342/NTU202500706

doi:10.6342/NTU202500706

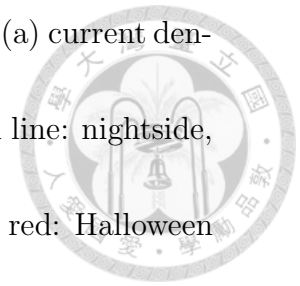

doi:10.6342/NTU202500706

List of Tables

doi:10.6342/NTU202500706

Chapter 1

Introduction

Space weather plays an important role in the diurnal variation of magnetosphere and ionosphere, hence impacts the human activities in the atmosphere and on the ground [1]. Power grids and transformers on the ground are vulnerable to the geomagnetically induced electric field (GIE) and the accompanied geomagnetically induced current (GIC). Ferocious space weather events strongly disturb the ionosphere, wreaking impairment on communication and navigation systems [2], [3], [4], [5]. The atmosphere may also be perturbed to interfere satellite operations [6], [7]. For example, 38 Starlink satellites were lost because of a geomagnetic storm on 4 February 2022 [1], [6]. Understanding the transient response in the ionosphere and on the ground level in the wake of space weather change is in urgent need, considering the heavy reliance of modern societies on electronic devices.

The solar wind and accompanied interplanetary magnetic field (IMF) drive field-aligned currents (FACs), which in turn induce GIE and GIC on the Earth surface [8], [9]. Strong

doi:10.6342/NTU202500706

GIC may damage the transformer [10], power grids, transmission lines, railway equipment, communication cables and pipeline networks [1], [11], [12].

The geomagnetic disturbance is dominated by the ionospheric currents and FACs, augmented by the currents in the conducting ground [9]. The geomagnetic disturbance $\Delta\bar{B}$ caused by ionospheric currents and FACs, $\bar{J}(\bar{r}')$, can be represented as $\Delta\bar{B} = \nabla \times \bar{A}$, with a vector potential [13]

$$\bar{A}(\bar{r}) = \frac{\mu}{4\pi} \int_V \frac{\bar{J}(\bar{r}') e^{-jk|\bar{r}-\bar{r}'|}}{|\bar{r}-\bar{r}'|} dV \tag{1.1}$$

where $\bar{r}$ is the observer position, $\bar{r}'$ is the position of current source, $k = \sqrt{\omega^2 - \omega_p^2}/c$ is the electromagnetic (EM) wavenumber in plasmas, c is the speed of light, ω is the angular frequency of EM waves, $\omega_p = \sqrt{4\pi n q_e^2/m_e}$ is the plasma frequency, n is the number density of particles, q_e is the elementary charge, and m_e is the electron mass [14].

The electric field is given by [13]

$$\bar{E}(\bar{r}) = -\nabla\Phi(\bar{r}) - j\omega\bar{A}(\bar{r}) \tag{1.2}$$

where Φ is a scalar potential accounting for the accumulated charge, which in turn depends on the conductivity contrast between continental and ocean regions, or on inland conductivity anomalies [9].

Behaviors of FAC, GIE and GIC are chaotic and difficult to predict [9], [15], [16]. In [15], predictions of geomagnetic field perturbations were made by using 14 different models and

doi:10.6342/NTU202500706

verified with observation at 12 different locations. The performances of these models were evaluated with five different metrics. In [16], the performance of Space Weather Modeling Framework (SWMF) in predicting geomagnetic field perturbations and their time rate of change was studied. Different components of perturbations manifested different characteristics and the performance varied with position.

The Earth magnetospheric response to solar wind has been studied [17], [18]. In [17], a global magnetohydrodynamic (MHD) model was used to simulate the responses of the Earth magnetosphere to solar wind. The dynamics of the Earth magnetosphere under steady solar wind with northward interplanetary magnetic field (IMF) were presented. In [18], the tilt angle of geomagnetic field and the polarity of solar wind were included in the model. In [17] and [18], the inner boundary of computational domain is set at $3R_e$, with R_e the Earth radius. Pushing the inner boundary closer to Earth will lead to unacceptably small time step in MHD simulations because of the higher magnetic field and associated Alfven speed closer to the Earth [19].

The behaviors of ionosphere can be described by applying empirical models, physical-based models and parameterized models, respectively [20], [21], [22], [23]. The thermosphere variations were simulated for a reference case, a storm with geomagnetic energy enhancement, and a storm with both solar and geomagnetic energy enhancement by using a global

doi:10.6342/NTU202500706

ionosphere−thermosphere model (GITM) [20], [24]. The hydrodynamics in vertical direction was accounted for with a vertical momentum equation. The plasma density, wind velocity and vertical wind at altitude of 400 km were compared and analyzed.

The GIE and associated GIC at ground level were studied in the literature [25], [26]. In [25], the frequency-domain GIE around Japan was simulated, assuming a current source flew at 10 Earth radii and the magnetospheric plasma was ignored. In [26], the GIE around Japan was simulated by applying a 3D finite-difference time-domain (FDTD) method. Then, the GICs flowing in a simplified 500 kV power grid were computed by using a Lehtinen−Pirjola method [27], [28]. A current sheet in the ionospherie was estimated from the measured magnetic field perturbation on 27-28 May 2017, after being low-pass filtered to remove frequency components higher than 10 mHz. Some match with the observation was found on electric field components and GICs, while short-time fluctuations were not reproduced in the simulations [29].

In [30], the relationship between dB/dt measured by ground-based magnetometers and FAC of AMPERE data was analyzed. In the storm on 22 June 2015, few spikes of dB/dt were observed before the arrival of the main pressure pulse. Most spikes were observed on the dayside between 08h and 16h magnetic local time (MLT). In general, the FACs expand equatorwards and the spikes move polewards. The spikes were correlated in location with the

doi:10.6342/NTU202500706

FACs. In the storm on 9 March 2012, most spikes were observed on the nightside between 21h and 03h MLT. A large number of spikes appeared in the region with upwards FAC.

In previous studies on GIE, the current sources inducing GIE and their waveforms were simply assumed as a sinusoidal current sheet or line current in the literature [25], [26], [30]. The relationship between the FACs flowing in ionosphere / magnetosphere and the GIE on the Earth surface is still elusive.

In this work, the FAC-induced GIE on the Earth surface is simulated and analyzed, under magnetic storms comparable to four scenarios and geophysical parameters around Japan. The magnetospheric responses to solar wind are simulated by applying an MHD model. Then, the behavior in the ionosphere is simulated, with the boundary conditions derived from the magnetospheric responses. The distributions of GIE are simulated by applying an FDTD method on the current sources derived from the ionospheric simulations.

The rest of this work is organized as follows. The MHD model of solar winds is presented in Section 2, the FDTD model for computing FAC-induced GIE is presented in Section 3, simulations on FAC and GIE are analyzed in Section 4, and some conclusions are drawn in Section 5.

doi:10.6342/NTU202500706

Chapter 2

MHD Model of Solar Winds

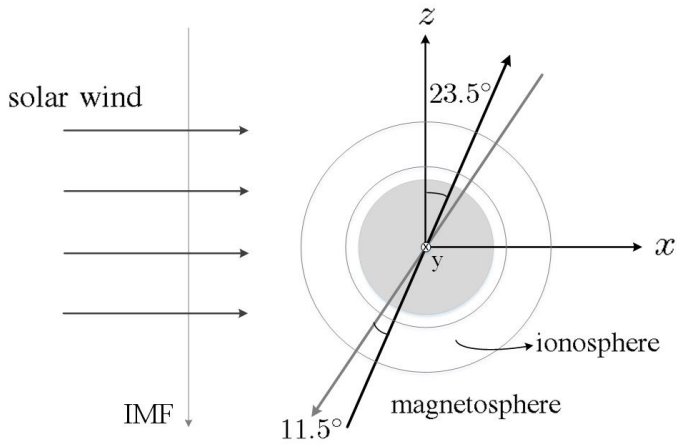

Figure 2.1: Configuration of solar winds blowing on Earth.

Fig.2.1 shows the configuration of solar winds blowing on Earth [18]. The Earth is centered at the origin, orbiting on the xy plane, and the sun is located in $-x$ direction. The Earth rotation axis, which is marked by a black arrow, tilts by 23.5° from the z axis. The dipole axis of geomagnetic field, which is marked by a grey arrow, tilts by 11.5° from the rotational axis. The solar wind blows into the computational domain from $-x$ direction. A southward IMF in December is considered, which induces the strongest FAC and disturbance

doi:10.6342/NTU202500706

[18].

The normalized MHD equations for modeling the solar winds are given by [18]

$$\frac{\partial \rho}{\partial t} + \nabla \cdot (\rho \bar{v}) = 0 \tag{2.1}$$

$$\frac{\partial}{\partial t}(\rho \bar{v}) + \nabla \cdot (\rho \bar{v}\bar{v} + p_t \bar{\bar{I}} - \bar{B}\bar{B}) = 0 \tag{2.2}$$

$$\frac{\partial E}{\partial t} + \nabla \cdot [(E + p_t)\bar{v} - \bar{B}(\bar{v} \cdot \bar{B})] = 0 \tag{2.3}$$

$$\frac{\partial \bar{B}}{\partial t} = \nabla \times (\bar{v} \times \bar{B}) \tag{2.4}$$

where ρ is mass density, $\bar{v}$ is velocity, $\bar{B}$ is magnetic field, $E = e + \rho|\bar{v}|^2/2 + B^2/2$ is total energy density, p is gas pressure, $e = p/(\gamma - 1)$ is internal energy density, $\gamma = 5/3$ is the ratio of specific heats and $p_t = p + B^2/2$ is total pressure.

The normalization factors are chosen as $L_0 = R_e = 6371$ (km), $n_0 = 10^4$ (1/cm^3), $\rho_0 = n_0 m_0 = 1.67 \times 10^{-20}$ (g/cm^3), $p_0 = 7.74 \times 10^{-3}$ (dyn/cm^2), $v_0 = \sqrt{p_0/\rho_0} = 6807$ (km/s), $B_0 = \sqrt{4\pi\rho_0 v_0^2} = 0.312$ (Gauss), $t_0 = L_0/v_0 = 0.936$ (s) and $T_0 = N_0 p_0/(2n_0 R) = 2.8 \times 10^9$ (K), where $m_0 = 1.67 \times 10^{-24}$ (g) is the mass of a proton, $R = 8.314 \times 10^7$ (erg/mol/K) and $N_0 = 6.02 \times 10^{23}$ is the Avogadro number [18], [31].

The Earth ionosphere and lower magnetosphere contain low-β plasma [32]. Implementation with the full conservative formalism in (2.1)-(2.4) may arouse huge round-off error on p if $\beta = 2p/|\bar{B}|^2 \ll 1$. In that case, we adapt the gas dynamic conservative formalism, which

doi:10.6342/NTU202500706

is physically equivalent to (2.1)-(2.4), as [18], [33]

$$\frac{\partial \rho}{\partial t} + \nabla \cdot (\rho \bar{v}) = 0 \tag{2.5}$$

$$\frac{\partial}{\partial t}(\rho \bar{v}) + \nabla \cdot (\rho \bar{v}\bar{v} + p\bar{\bar{I}}) = \bar{J} \times \bar{B} \tag{2.6}$$

$$\frac{\partial E^{\mathrm{hd}}}{\partial t} + \nabla \cdot [(E^{\mathrm{hd}} + p)\bar{v}] = \bar{J} \cdot \bar{E} \tag{2.7}$$

$$\frac{\partial \bar{B}}{\partial t} = \nabla \times (\bar{v} \times \bar{B}) \tag{2.8}$$

where $E^{\mathrm{hd}} = e + \rho|\bar{v}|^2/2$, $\bar{J} = \nabla \times \bar{B}$ and $\bar{E} = -\bar{v} \times \bar{B}$. Note that the conservative quantities $[\rho, \rho\bar{v}, E]$ are adopted in (2.1)-(2.4), while $[\rho, \rho\bar{v}, E^{\mathrm{hd}}]$ are adopted in (2.5)-(2.8).

An in-house MATLAB code was developed to solve the MHD equations [18], [31]. The code is based on the Godunov-type finite-volume algorithm with HLL-type Riemann solvers and slope limiters [34]. A constrained transport method was applied to maintain the divergence-free condition of magnetic field [35]. On the outer boundaries, inflow boundary conditions are imposed at the dayside, and outflow boundary conditions are imposed otherwise. On the inner boundary, the magnetosphere-ionosphere (MI) coupling, which affects the magnetospheric convection, is adopted [17], [18].

The initial conditions in the computational domain are set as follows: The particle number density is proportional to $1/r^3$ and is $n = 28$ $(1/\mathrm{cm}^3)$ at $r = 3R_e$ [18], [36]. The temperature is $T = 1510$ (K) at $r = 3R_e$. The gas pressure at $r = 3R_e$ is determined by the ideal gas law and is proportional to $1/r^2$.

doi:10.6342/NTU202500706

In 3D simulations, the geomagnetic field is represented in terms of a potential field as [37], [38]

$$\bar{B} = -\nabla\psi \ \ (\text{nT}) \tag{2.9}$$

where

$$\psi = R_e \sum_{n=1}^{\infty} \left(\frac{R_e}{r}\right)^{n+1} \sum_{m=0}^{n} [g_n^m \cos(m\phi) + h_n^m \sin(m\phi)] P_n^m(\cos\theta) \tag{2.10}$$

$$P_n^m(\mu) = \sqrt{\frac{(n-m)!(2-\delta_{0m})}{(n+m)!}} (1-\mu^2)^{m/2} \left(\frac{d}{d\mu}\right)^m P_n(\mu) \tag{2.11}$$

with the first term in (2.10) depicting a dipole field, $P_n(\mu)$ is Legendre function, and the coefficients of the first few terms are $g_1^0 = -29,877$, $g_1^1 = -1,903$, $g_2^0 = -2,073$, $g_2^1 = 3,045$, $h_1^1 = 5,497$ and $h_2^1 = -2,191$.

In 2D simulations, the magnetic field of a line dipole is used [39]

$$\bar{B} = \hat{x} D \frac{2xz}{r^4} + \hat{z} D \frac{z^2 - x^2}{r^4} \tag{2.12}$$

where $D = -3,110$ (nT) is the dipole moment. Note that the dipole moment adopted in 2D simulations is about 10 times smaller than that of the geomagnetic field, and it decays with r more slowly than that of the geomagnetic field. The position of magnetopause in 2D simulations is comparable to that in 3D simulations. The 2D simulations are used to mimic the behaviors of 3D simulations on the meridian plane.

doi:10.6342/NTU202500706

Table 2.1: Parameters associated with solar wind.

Case	$n_{\rm sw}$ $(1/{\rm cm}^3)$	$v_{\rm sw}$ (km/s)	$T_{\rm sw}$ (K)	$B_{\rm sw}$ (nT)
steady solar wind [17], [18], [24]	5	400	2×10^5	5
May 2017 storm [40], [41]	10	400	1×10^6	20
Halloween storm [42]	15	1,800	1×10^7	50
Carrington storm [43], [44]	40	1,800	1×10^7	65

The inflow boundary conditions on solar wind are given by [17], [18]

$$\rho = \rho_{\rm sw}, \quad v_x = v_{\rm sw}, \quad T = T_{\rm sw}, \quad B_z = B_{\rm sw} \tag{2.13}$$

Table 2.1 lists the parameters associated with four scenarios of solar wind, including the steady solar wind, the May 2017 storm, the Halloween storm and the Carrington storm [17], [18], [24], [42], [40], [41], [43], [44]. The steady solar wind represents the typical values under the normal situation [17], [18], [24]. The quasi-equilibrium state under steady solar wind is used as the initial condition in each simulation of solar storm.

On May 27-28, 2017, an intense GIE in Japan due to geomagnetic storm was recorded [26], [40], [41]. The associated velocity of solar wind was about 400 (km/s), and the magnitude of IMF was about 20 (nT) [40], [41]. The particle number density and temperature of the solar wind were not reported, but can be inferred from the parameters of similar storms. Compared with the steady solar wind and the Halloween storm, the particle number density and temperature of the May 2017 storm are inferred as $n_{\rm sw} = 10$ $(1/{\rm cm}^3)$ and $T_{\rm sw} = 10^6$ (K), respectively.

doi:10.6342/NTU202500706

In late October 2003, three massive sunspot groups, accompanied with 17 major solar flares, emerged on the solar surface, causing the Halloween solar storms [42], [45]. Two high solar wind speeds were recorded at $v_{\rm sw} \simeq 1,850$ km/s on October 29and $v_{\rm sw} \simeq 2,240$ km/s on October 30 [42]. The proton number density increased to about 15 ($1/\text{cm}^3$). The temperature of the solar wind increased to about 1.25×10^7 K in the first storm, and about 5×10^6 in the second storm. The interplanetary magnetic field (IMF) was about -60 nT on October 29 and -40 nT on October 30. The solar flare intensity was X28 (2.8×10^{-3} W/m^2) on October 29 and X17 (1.7×10^{-3} W/m^2) on October 30 [45].

The notorious Carrington storm [24], [43], [44], [46] is also simulated in this work. The intensity of horizontal magnetic field of $-1,600$ nT was recorded at Mumbai, India [24], [43], [46]. The disturbance-storm time (Dst) index was estimated as -850 nT [43]. The leading edge velocity of the interplanetary coronal mass ejection (ICME) was about 1,900 km/s [43]. The magnetic field was matched by a solar storm model with IMF of 65 nT and solar wind density of 40 $1/\text{cm}^3$ [46], associated with solar flare intensity of X80 (8×10^{-3} W/m^2) [44].

On the inner boundary, the mass density, gas pressure, normal velocity component and magnetic field are fixed at their initial values. The tangential velocity of plasma on the inner boundary is determined via the MI coupling, which is elaborated in Section 2.1.

doi:10.6342/NTU202500706

2.1 Magnetosphere-Ionosphere Coupling on Inner Boundary

The inner boundary for global MHD simulations is typically chosen at several R_e because of the increased magnetic field and associated Alfven speed near the Earth [19]. When the Alfven speed increases, the time-step in MHD simulation decreases and reaches an unacceptable small value around the Earth. Hence, the magnetosphere-ionosphere (MI) coupling is implemented on the inner boundary of global MHD simulation [17], [18], [19]. The interface between the ionosphere and magnetosphere follows Ohm's law boundary condition [19]. The ionosphere serves as a resistor, which regulates currents in the magnetosphere and significantly affects the magnetospheric convection [17], [19].

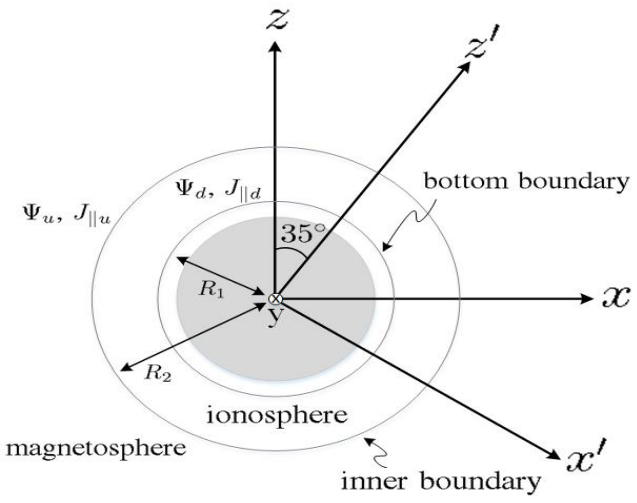

Figure 2.2: Schematic of magnetosphere-ionosphere coupling.

Fig.2.2 shows the schematic of magnetosphere-ionosphere (MI) coupling. Define a co-

doi:10.6342/NTU202500706

ordinate system (x, y, z), with xy plane being the plane of the ecliptic, and a coordinate system (x', y', z'), with z' aligning with the dipole axis [18]. The rotational axis tilts by 23.5° from the z axis and the dipole axis tilts by 11.5° from the rotational axis. Hence, the coordinates (x', y', z') is determined by rotating (x, y, z) by 35° about the y-axis. Note that the y'-axis aligns with the y-axis. When simulating the magnetospheric response, the solar wind blows into the computational domain from an outer boundary at $-x$ direction, and the computational domain is truncated on the inner boundary. When simulating the ionospheric response, the computational domain extends from the bottom boundary to the inner boundary, in which the boundary at $R = 1.013R_e = 80$ (km) is the bottom boundary and the inner boundary is adaptive, according to the requirement of the scenarios.

The inner boundary is treated as a 2D shell, which is described by the coordinates (θ, ϕ), where

$$\theta = \cos^{-1} \frac{z'}{\sqrt{x'^2 + y'^2 + z'^2}} \tag{2.14}$$

$$\phi = \text{sign}(y') \cos^{-1} \frac{x'}{\sqrt{x'^2 + y'^2}} \tag{2.15}$$

The field aligned current and the ionospheric potential on the bottom boundary at $R = R_1$ are $J_{\parallel d}$ and Ψ_d, respectively. The field aligned current and the ionospheric potential on the inner boundary at $R = R_2$ are $J_{\parallel u}$ and Ψ_u, respectively. In this work, $R_1 = 1.013R_e$ and $R_2 = 3R_e$.

doi:10.6342/NTU202500706

The magnetosphere-ionosphere (MI) coupling on the inner boundary is implemented in five steps [18]

(1) Compute the field-aligned current (FAC) density on the inner boundary as

$$J_{\parallel u}(\theta, \phi) = (\nabla \times \bar{B}) \cdot \hat{b} \tag{2.16}$$

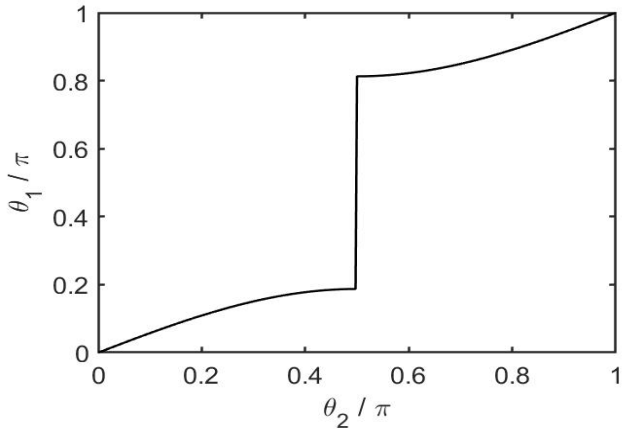

Figure 2.3: Relation between θ_1 and θ_2, with $(R_1, R_2) = (1.013R_e, 3R_e)$ [19].

(2) (2) Map the FAC current density from the inner boundary to the bottom boundary along the geomagnetic field line as [18], [19]

$$J_{\parallel d}(\theta_1, \phi_1) = \left(\frac{R_2}{R_1}\right)^3 \left(\frac{1 + 3\cos^2\theta_1}{1 + 3\cos^2\theta_2}\right)^{1/2} \times J_{\parallel u}(\theta_2, \phi_2) \tag{2.17}$$

where

$$\theta_1 = \sin^{-1}\left(\frac{R_1 \sin^2\theta_2}{R_2}\right)^{1/2}$$

$$\phi_1 = \phi_2$$

doi:10.6342/NTU202500706

Fig.2.3 shows the relation between θ_1 and θ_2, with $(R_1, R_2) = (1.013R_e, 3R_e)$. The magnetic field lines cross (R_2, θ_2, ϕ_2) in the northern hemisphere ($\theta_2 < \pi/2$) intersect with the bottom boundary at $\theta_1 < 33.7°$. The magnetic field lines cross in the southern hemisphere ($\theta_2 > \pi/2$) intersect with the bottom boundary at $\theta_1 > 146.3°$.

(3) Compute the ionospheric potential $\Psi_d(\theta_1, \phi_1)$ on the bottom boundary. The ionospheric potential Ψ in the ionosphere varies slowly along the magnetic field lines because the conductivity parallel to $\bar{B}$ is large [19]. Hence, the ionospheric potential $\Psi(r = R_1)$ is approximated as a 2D shell on the bottom boundary as [17], [18], [33]

$$J_{\parallel d}(\theta_1, \phi_1) \cos\delta = \nabla_S \cdot (\bar{\bar{\Sigma}} \cdot \nabla_S \Psi_d) \tag{2.18}$$

where

$$\bar{\bar{\Sigma}} = \begin{bmatrix} \sigma_p/\cos^2\delta & -\sigma_h/\cos\delta \\ \sigma_h/\cos\delta & \sigma_p \end{bmatrix}$$

is the ionospheric conductance tensor and , $\sigma_p = 5$ (S) and $\sigma_h = 0$ are the Pedersen conductance and the Hall conductance, respectively, and $\cos\delta = -2\cos\theta/\sqrt{1+3\cos^2\theta}$ is the angle between $\hat{b}$ and $\hat{r}$. Eqn.(2.18) is the Kirch-hoff's current law. The current flowing on the bottom boundary satisfy

$$[J_\theta, J_\phi]^t = -\bar{\bar{\Sigma}} \cdot \nabla_S \Psi_d \tag{2.19}$$

and the divergence of current flowing on the $r = R_1$ shell is equal to the FAC flowing onto

doi:10.6342/NTU202500706

the bottom boundary.

The gradient of ionospheric potential is represented as

$$\nabla_S \Psi_d = \left[\hat{\theta} \frac{1}{r} \frac{\partial \Psi_d}{\partial \theta} + \hat{\phi} \frac{1}{r \sin\theta} \frac{\partial \Psi_d}{\partial \phi} \right] \tag{2.20}$$

By substituting (2.20) into (2.18), (2.18) can be rewritten as

$$\begin{aligned} J_{\parallel d}(\theta_1, \phi_1) \cos\delta &= \nabla_S \cdot \left(\hat{\theta} \frac{\sigma_p}{\cos^2\delta} \frac{1}{r} \frac{\partial \Psi_d}{\partial \theta} + \hat{\phi} \frac{\sigma_p}{r \sin\theta} \frac{\partial \Psi_d}{\partial \phi} \right) \\ &= \frac{1}{r \sin\theta} \left[\frac{\partial}{\partial \theta} \left(\frac{\sigma_p}{\cos^2\delta} \frac{1}{r} \frac{\partial \Psi_d}{\partial \theta} \right) \cdot \sin\theta + \frac{\sigma_p}{\cos^2\delta} \frac{1}{r} \frac{\partial \Psi_d}{\partial \theta} \cdot \cos\theta \right] + \frac{1}{r \sin\theta} \frac{\partial}{\partial \phi} \left(\frac{\sigma_p}{r \sin\theta} \frac{\partial \Psi_d}{\partial \phi} \right) \\ &= \frac{\sigma_p}{r^2 \cos^2\delta} \frac{\partial^2 \Psi_d}{\partial \theta^2} + \frac{\sigma_p}{r^2} \frac{\partial \Psi_d}{\partial \theta} \frac{\partial}{\partial \theta} \left(\frac{1}{\cos^2\delta} \right) + \frac{\sigma_p \cos\theta}{r^2 \sin\theta \cos^2\delta} \frac{\partial \Psi_d}{\partial \theta} + \frac{\sigma_p}{r^2 \sin^2\theta} \frac{\partial^2 \Psi_d}{\partial \phi^2} \end{aligned} \tag{2.21}$$

which can be discretized as

$$\begin{aligned} \left(\frac{2\sigma_p}{r^2 \cos^2\delta \Delta\theta^2} + \frac{2\sigma_p}{r^2 \sin^2\theta \Delta\phi^2} \right) \Psi_{dmn} &= \frac{\sigma_p}{r^2 \cos^2\delta} \frac{\Psi_{d(m+1)n} + \Psi_{d(m-1)n}}{\Delta\theta^2} \\ &+ \left[\frac{\sigma_p}{r^2} \frac{\partial}{\partial \theta} \left(\frac{1}{\cos^2\delta} \right) + \frac{\sigma_p \cos\theta}{r^2 \sin\theta \cos^2\delta} \right] \frac{\Psi_{d(m+1)n} - \Psi_{d(m-1)n}}{2\Delta\theta} + \frac{\sigma_p}{r^2 \sin^2\theta} \\ &\frac{\Psi_{dm(n+1)} + \Psi_{dm(n-1)}}{\Delta\phi^2} - J_{\parallel dmn} \cos\delta \end{aligned} \tag{2.22}$$

where $\Psi_{mn} = \Psi[(m - 0.5)\Delta\theta, (n - 0.5)\Delta\phi]$.

(4) Map the ionospheric potential Ψ_d from the bottom boundary to the inner boundary along the geomagnetic field line. The mapping is implemented as [18], [19]

$$\Psi_u(\theta_2, \phi_2) = \Psi_d(\theta_1, \phi_1) \tag{2.23}$$

doi:10.6342/NTU202500706

(5) Determine the tangential velocity of plasma on the inner boundary as [18]

$$\bar{v} = \frac{\bar{E} \times \bar{B}}{|\bar{B}|^2} \tag{2.24}$$

where

$$\bar{E} = -\nabla_S \Psi_u \tag{2.25}$$

2.2 Simulations of Ionosphere

After the simulations of the magnetospheric response to the solar winds reach quasi-equilibrium states, the results are used to simulate the ionospheric response. In the simulations of ionosphere, the computational domain extends from the bottom boundary to the inner boundary, where the bottom boundary is at $R = 1.013R_e = R_e + 80$ (km). The boundary conditions on the inner boundary are set to the results of the simulations of magnetospheric response, and fixed boundary conditions are imposed on the bottom boundary. The initial condition of magnetic field within the inner boundary follows (2.9) for 3D simulations, and (2.12) for 2D simulations.

The vertical distribution of particle number density and temperature is specified by the data of International Reference Ionosphere (IRI) model [21]. Fig.2.4 shows the vertical distribution of particle number density and temperature, respectively [21]. The particle number density in the simulations is the summation of the number density of each kind of

doi:10.6342/NTU202500706

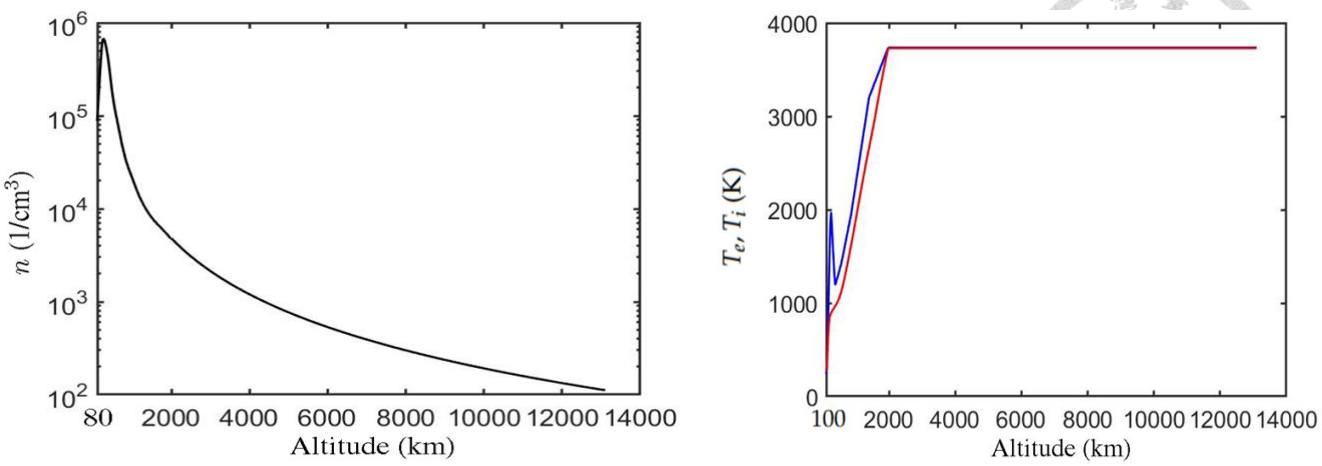

(a) (b)

Figure 2.4: Vertical distribution of particle number density, electron temperature and ion temperature, respectively, (a) n (1/cm^3), extracted from IRI model [21], (b) blue line: T_e [21], red line: T_i [21].

particles included in the IRI model. The temperature of the plasma is the average of the electrons and ions. Note that the IRI model only available in $80 < h < 2,000$ (km), where h is the altitude. Above $2,000$ (km), the particle number density is assumed to be proportional to $n \propto (h/2,000)^{-2}$ (in units of km), and the temperature is the same as that at $2,000$ km. When the simulations begin, the temperature will soon be heated due to the dissipation of magnetic field, leading to increased gas pressure and associated temperature. Although the gas pressure is increased, the magnetic pressure is much higher than the gas pressure. Hence, the plasma dynamics is dominated by the magnetic field, and the influence of gas pressure is insignificant.

doi:10.6342/NTU202500706

Chapter 3

FAC-Induced GIE with FDTD Method

GIE is induced by the FACs at Earth's surface through the induction [8], [9]. In this work, the evolution of GIE is simulated by using the FDTD method, with the currents sources obtained from the MHD simulations in section 2.

Fig.3.1 shows the schematic of the FDTD simulations. The computational domain extends from $-100 < z < 110$ (km), and in the range of $(25°N, 125°E)$, $(25°N, 150°E)$, $(50°N, 125°E)$ and $(50°N, 150°E)$. The $+x$ direction is towards the East and the $+y$ direction is towards the North. The 3D finite-difference time-domain (FDTD) method is applied to simulate the electrodynamics of the Earth-ionosphere system [26]. Source currents, extracted from the MHD simulations, are used to excite the electric and magnetic fields. Follow [26], the conductivities in the computational domain are divided into the air, seawater, sediment layer and basement rock layer, with conductivity $\sigma_a^e = 0$ (S/m), $\sigma_w^e = 2.5$ (S/m), $\sigma_s^e = 0.01$ (S/m) and $\sigma_r^e = 0.001$ (S/m), respectively. An absorption boundary con-

doi:10.6342/NTU202500706

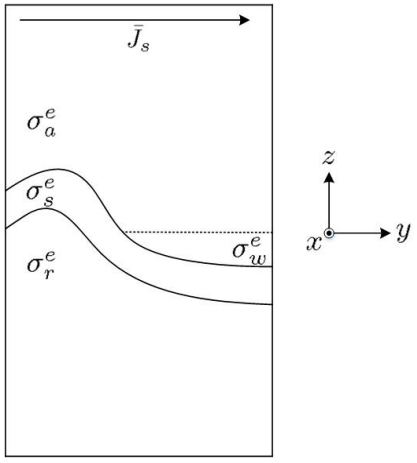

Figure 3.1: Schematic of FDTD simulations. The computational domain extends from $-100 < z < 110$ (km), and in the range of $(25°N, 125°E)$, $(25°N, 150°E)$, $(50°N, 125°E)$ and $(50°N, 150°E)$. Source currents, extracted from the MHD simulations, are used to excite the electric and magnetic fields. The conductivities in the computational domain are divided into the air, seawater, sediment layer and basement rock layer, with conductivity $\sigma_a^e = 0$ (S/m), $\sigma_w^e = 2.5$ (S/m), $\sigma_s^e = 0.01$ (S/m) and $\sigma_r^e = 0.001$ (S/m), respectively. An absorption boundary, convolutional perfect matched layer (CPML), is imposed around the computational domain. The $+x$ direction is towards the East and the $+y$ direction is towards the North.

dition, convolutional perfect matched layer (CPML), is imposed around the computational domain [49]. Note that the FDTD method and CPML absorption boundary condition are presented in Appendix I. The conventional FDTD method is limited by Courant-Friedrich-Levy (CFL) condition [49]. Typical geomagnetic storm electromagnetic fields (GS-EMFs) are characterized by ultralow frequencies, leading to large number of iterations to reach the duration of the geomagnetic storms [50], [51]. Hence, an acceleration technique, based on the Barycentric−Lagrange extrapolation, is proposed to acceleration the simulations.

doi:10.6342/NTU202500706

The FDTD algorithm starts from Maxwell's time-domain equations [26], [49]

$$\nabla \times \bar{H} = \epsilon \frac{\partial \bar{E}}{\partial t} + \bar{J} \tag{3.1}$$

$$\nabla \times \bar{E} = -\mu \frac{\partial \bar{H}}{\partial t} \tag{3.2}$$

where

$$\bar{J} = \bar{J}_c + \bar{J}_i = \sigma^e \bar{E} + \bar{J}_s \tag{3.3}$$

$\bar{J}$ is the current density, σ^e is the electric conductivity, $\bar{J}_s$ is the source current density, ϵ is the permittivity and μ is the permeability. The source current density is assumed as an uniform sheet current, which can be a superposition of sinusoidal functions or a function of time according to observation [26].

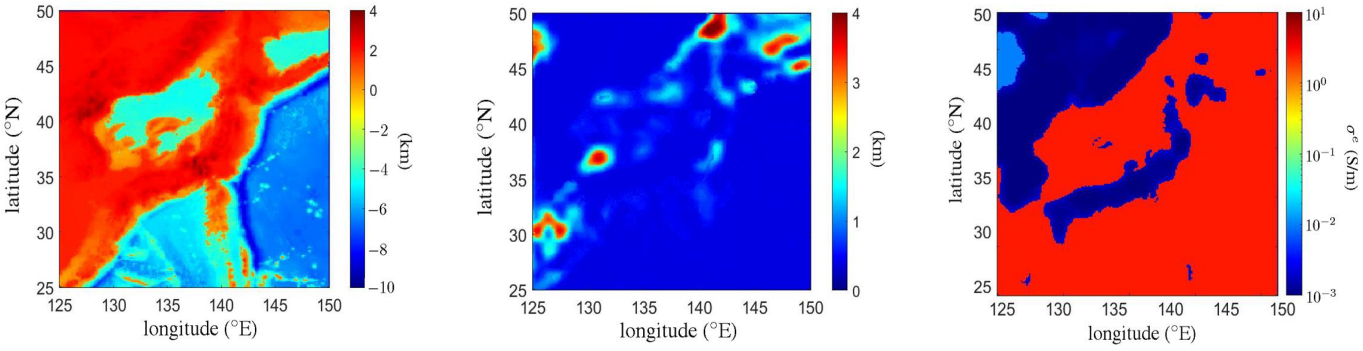

Figure 3.2: Topography of ETOPO1 global relief model from National Oceanic and Atmospheric Administration National Centers for Environmental Information, sediment thickness and averaged conductivity distribution in and around Japan [26], (a) topographic map [52], (b) sediment thickness [53], (c) averaged conductivity distribution from the surface to 1km beneath the ground [25].

The electrical conductivity σ^e is set according to the medium. The computational do-

doi:10.6342/NTU202500706

main is divided into the air, seawater, sediment layer and basement rock layer, and their conductivity are assumed as 0, 2.5, 10^{-2} and 10^{-3} (S/m), respectively [26]. Fig.3.2 shows the topographic map, sediment thickness and conductivity in and around Japan, in the range of $(25°N, 125°E)$, $(25°N, 150°E)$, $(50°N, 125°E)$ and $(50°N, 150°E)$ [52], [53], [26]. Fig.3.2(a) shows the topographic map corresponding to the computational domain. A deep-sea appears in the east direction of the main Japan island, and a relatively shallow sea with depth less than 1 km appears in the west direction of it. Fig.3.2(b) shows the sediment thickness corresponding to the computational domain. In general, the sediment layer has thickness of 0.2-0.4 km, except for some anomalies.

Fig.3.2(c) shows the averaged conductivity distribution from the surface to 1km beneath the ground [25]. The conductivity of a grid is the averaged by the conductivities in different medium if more than one type of medium appear in the grid. The conductivity at the grid $[m, n, \ell]$ is averaged as

$$\sigma^e_{mn\ell} = \frac{d_{wmn\ell}}{d_{mn\ell}}\sigma^e_w + \frac{d_{smn\ell}}{d_{mn\ell}}\sigma^e_s + \frac{d_{rmn\ell}}{d_{mn\ell}}\sigma^e_r \tag{3.4}$$

where d_w, d_s and d_r are the thicknesses of the seawater, sediment layer and basement rock layer, respectively, included in the grid and d is the depth of the mesh.

doi:10.6342/NTU202500706

Chapter 4

Results and Discussions

4.1 Simulations with 2D-MHD Model

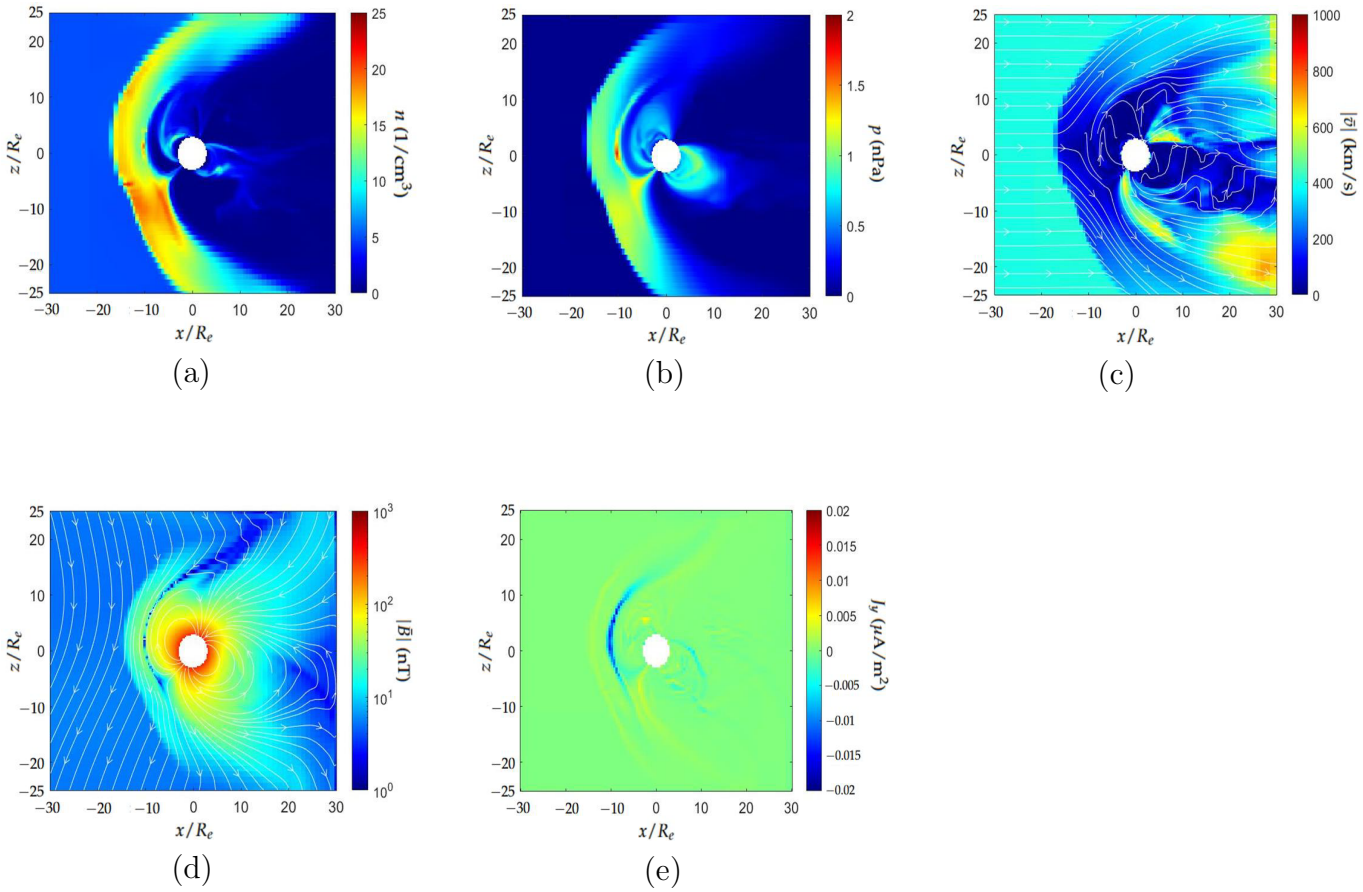

Figure 4.1: Distributions of plasma variables, magnetic field and current density of magnetosphere around the Earth at $t' = 800$ ($t = 750$ s), (a) n, (b) p, (c) $\bar{v}$, (d) $\bar{B}$, (e) J_y. The streamlines in (c) and (d) represent the direction of plasma flow and magnetic field lines, respectively. Note that the prime notation represents the normalized variable.

doi:10.6342/NTU202500706

Fig.4.1 shows the distributions of plasma variables, magnetic field and current density of magnetosphere around the Earth at $t' = 800$ ($t = 750$ s). At $t' = 800$ ($t = 750$ s), the simulation of steady solar wind reaches a quasi-equilibrium state. The steady solar wind, with a southward IMF, blows into the computational domain from $-x$ boundary. The particle number density accumulates at the dayside to form a high-pressure bow shock at $x \simeq -15R_e$, with $n \simeq 20$ (1/cm^3) and $p \simeq 1$ (nT). Some plasmas flow out from the inner boundary at the north and south poles. The geomagnetic field on the dayside is compressed by the solar wind, and some of the magnetic field lines reconnect. A strong current density is induced around the bow shock.

Fig.4.2 shows the distributions of plasma variables, magnetic field and current density of magnetosphere around the Earth under Carrington storm. In this case, the altitude of the inner boundary is decreased to $R = 1.013R_e$, namely, the simulations of magnetosphere and ionosphere are merged to one simulation. Fig.4.2(a) shows that at the dayside, the solar wind with high particle number density blows towards the Earth, with $n = 40$ (1/cm^3). The bow shock is compressed, compared with that under steady solar wind, as in Fig.4.1(a). Fig.4.2(b) shows that the gas pressure increases to about 100 (nPa) on the bow shock due to intense solar wind. Fig.4.2(c) shows the velocity of plasma flow. The speed of the solar wind is $1,800$ (km/s), and the speed around the Earth is much slower than that of the solar

doi:10.6342/NTU202500706

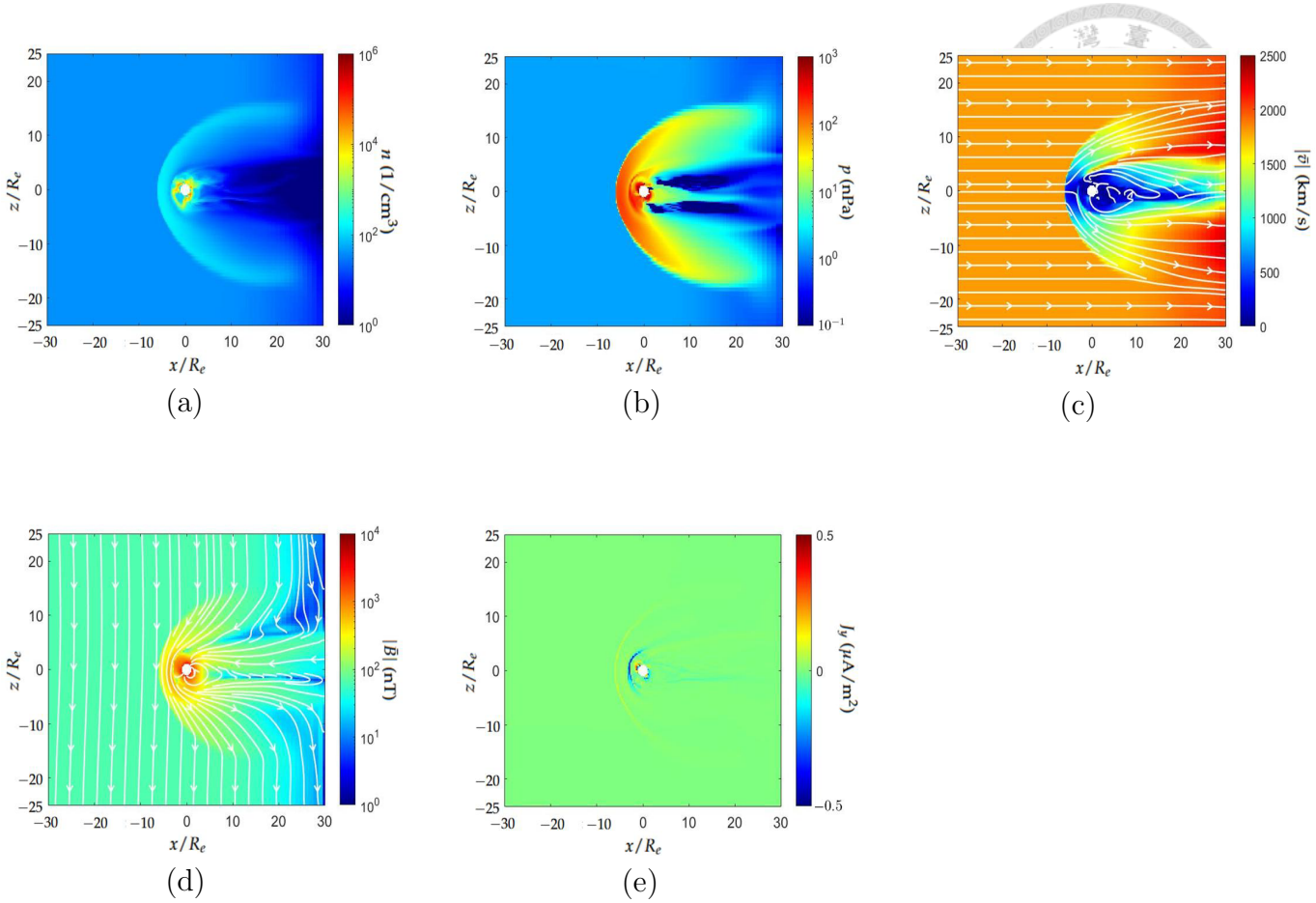

Figure 4.2: Distributions of plasma variables, magnetic field and current density of magnetosphere around the Earth under Carrington storm, (a) n, (b) p, (c) $\bar{v}$, (d) $\bar{B}$, (e) J_y. The streamlines in (c) and (d) represent the direction of plasma flow and magnetic field lines, respectively.

wind. Fig.4.2(d) shows the distribution of magnetic field. The magnetopause is compressed along with the bow shock, and a magnetotail is formed at the nightside. Fig.4.2(e) shows the distribution of the current density. The current flowing around the bow shock is observed, and the magnitude is increases significantly to about 0.5 (μA/m^2).

Fig.4.3 shows the comparison of the current density distributions in magnetosphere under steady solar wind, 2017 storm, Halloween storm and Carrington storm. Fig.4.3(a) shows the

doi:10.6342/NTU202500706

distribution of current density distribution under steady solar wind. The magnitude of the current density is about 0.01 (μA/m^2) at the dayside. Fig.4.3(b) shows that under the May 2017 storm, the magnitude of the current density increases to about 0.03 (μA/m^2), which is marked by the red arrow. The geomagnetic field is further compressed at the dayside to induce current density, which is encircled by the red contour. Fig.4.3(c) shows that under the Halloween storm, the bow shock is compressed significantly, and the magnitude of the bow shock is increases to about 0.5 (μA/m^2). Fig.4.3(d) shows that under the Carrington storm, the current density is further enhanced, and the location with high current density becomes further closer to the Earth.

Fig.4.4 shows the distribution of plasma variables, magnetic field and current density, respectively, under steady solar wind within $3R_e$ at $t' = 80$ ($t = 75$ s). Fig.4.4(a) shows that the particle number density is higher around the Earth, and decreases outwards, as in Fig.2.4(a). Mild perturbation is observed in the ionosphere. Fig.4.4(b) shows that the gas pressure is high around the Earth. In addition, the distribution of gas pressure towards equatorward is heated to have higher gas pressure. The detail of gas pressure will be discussed in Fig.4.5. Fig.4.4(c) shows the distribution of plasma flow. In general, the magnitude of the velocity is $|\bar{v}| \simeq 50$ (km/s), and the direction of plasma flow is along the magnetic field lines. The velocity around the inner boundary ($3R_e$) is larger because the plasma is

doi:10.6342/NTU202500706

affected by the plasma with higher gas pressure in the magnetosphere, as marked by the red arrow. The distributions of plasma variables in the magnetosphere are presented in Fig.4.1. Fig.4.4(d) shows the magnitude of total magnetic field and the magnetic field lines. No significant change is observed on the total magnetic field. Fig.4.4(e) shows the perturbation of magnetic field $\bar{B}_1 = \bar{B} - \bar{B}_e$, where $\bar{B}_e$ is the geomagnetic field. The distribution of magnetic field lines manifest two loops at the dayside and nightside, respectively, which are marked by the red contours. The perturbation of magnetic field $|\bar{B}_1|$ is about 2-3 orders smaller than the magnitude of total magnetic field $|\bar{B}|$. Fig.4.4(f) shows the distribution of current density J_y. In general, the distribution of J_y is highly correlated to the magnetic field lines. The current density at lower ionosphere is relatively larger, and that at high altitude is more significant at the equatorial direction. The magnitude of the current density is about 0.01 (μA/m^2), with a maximum of about 0.09 (μA/m^2), which is well fitted with the measured data in the range of $\pm$0.1 (μA/m^2) [48].

Fig.4.5 shows the distribution of gas pressure under steady solar wind within $3R_e$. At $t = 0$, the plasma in the ionosphere satisfies the conditions in Fig.2.4. The particle number density decreases drastically with the altitude, and the temperature increases mildly with the altitude. The plasma satisfies the ideal gas law as

$$p = \frac{\rho}{N_0 \mu m_p} RT \tag{4.1}$$

doi:10.6342/NTU202500706

where $N_0 = 6.02 \times 10^{23}$ is the Avogadro's number, m_p is the proton mass, $R = 8.314 \times 10^7$ (erg/mol/K) and $\mu = 0.5$ is the average particle weight, which assumes all the ions are hydrogen ions. A ring with high gas pressure appears around the Earth because the particle number density decreases significantly outwards. At $t' = 80$ ($t = 75$ s), the distribution of gas pressure towards equatorward is heated due to the dissipation of magnetic energy to have higher gas pressure. The heated region corresponds to the region with higher current density. At higher altitude, the particle number density is low, leading to significant heating.

Fig.4.6 shows the distribution of plasma variables, magnetic field and current density, respectively, under Carrington storm around the Earth. Fig.4.6(a) shows that the particle number density remains in the lower ionosphere, while large perturbations appear at higher altitude. Fig.4.6(b) shows that the gas pressure is further heated in the ionosphere, and the gas pressure is higher at the equatorial direction, as marked by the white contours. The large structure is similar to the magnetic field lines. Fig.4.6(c) shows that the magnitude of the velocity is increased. The direction of plasma flow manifest turbulent, while the large structure is similar to the magnetic field lines. Fig.4.6(d) and (e) show that the magnitude of total magnetic field and the magnetic field lines manifest no significant change, while the perturbation of magnetic field $\bar{B}_1$ is enhanced. The magnitude of $|\bar{B}_1|$ is much smaller than that of $|\bar{B}|$. The loop structure, observed under steady solar wind, is significantly disturbed

doi:10.6342/NTU202500706

during the Halloween storm. Fig.4.6(f) shows that the magnitude of current density J_y increases to about 0.1 (μA/m^2). The distribution of J_y is in general along the magnetic field lines. Compared with Fig.4.4(f), the current density under steady solar wind concentrates at lower latitude and lower altitude, and that under Carrington storm extends to higher latitude and higher altitude.

Fig.4.7 shows the comparison of current density distributions in ionosphere under steady solar wind, 2017 storm, Halloween storm and Carrington storm, respectively. Fig.4.7(a) shows that under the steady solar wind, the maximum of the current density is about 0.1 (μA/m^2). The current concentrates at equatorial direction. Fig.4.7(b) shows that under the May 2017 storm, the maximum of the current density increases to about 0.5 (μA/m^2). The current density at lower ionosphere increases significantly, and that at the dayside is stronger than that at the nightside, as encircled by the red contour. Fig.4.7(c) shows that under the Halloween storm, the maximum of $|J_y|$ increases to about 1 (μA/m^2). The current density in the ionosphere is enhanced. The current density around the north and south poles is enhanced because the plasma flows towards the Earth along the magnetic field lines. Fig.4.7(d) shows that under the Carrington storm, the maximum of the current density increases to about 1.5 (μA/m^2). In this case, the current density flowing in the ionosphere is significantly enhanced.

doi:10.6342/NTU202500706

Phenomena akin to the Van Allen radiation belts are revealed in the simulations. The Van Allen radiation belts, consisting of an inner and an outer belts, trap relativistic, non-thermal electrons and protons due to the Earth's magnetic field [54]. Typically, the inner belt extends from an altitude of $0.2R_e$-$2R_e$, and the outer belt extends from an altitude of $3R_e$-$10R_e$ [55]. Under strong solar activities, the locations of the belts may decline towards the Earth's surface.

Fig.4.8 shows the distributions of current density in the magnetosphere and ionosphere under steady solar wind and Carrington storm, respectively. Fig.4.8(a) shows that two belts appear in the magnetosphere, marked by two red arrows. The belt at the dayside concentrates at around $5R_e$, and that at the nightside extends from $3R_e$-$10R_e$, which are akin to the outer Van Allen radiation belt. Fig.4.8(b) shows that in the ionosphere, two belts, marked by two red arrows, appear at the dayside and nightside, respectively, and extend from the vicinity of the Earth to about $2R_e$, which are akin to the inner Van Allen radiation belt. Fig.4.8(c) shows that under the Carrington storm, the strong solar wind compresses the bow shock towards the Earth, and the outer belt moves to about $3R_e$. The inner belt is pushed towards the Earth's surface. Note that in the MHD simulations, the particle number density, kinetic energy and current density contain the thermal and non-thermal particles [56], [57]. The behaviors of relativistic, non-thermal particles of the Van-Allen radiation belts may be

doi:10.6342/NTU202500706

investigated if some observable physical quantities, such as radiation intensity and spectrum, are available.

4.2 GIE Induced by Current Sheet Obtained from the MHD Simulations

In the simulations of GIE, the current densities, derived from the global MHD simulations, at altitude of $h = 100$ (km) are recorded and interpolated as the current sources that inducing GIE at the Earth's surface. For an electromagnetic (EM) wave propagating in a plasma, the dispersion relation is given by [14]

$$k^2 = \frac{\omega^2 - \omega_p^2}{c^2} \tag{4.2}$$

where k is the wavenumber of the EM wave, $\omega_p = \sqrt{4\pi n q_e^2/m_e}$ is the plasma frequency, c is the speed of light, q_e is the elementary charge and m_e is the mass of an electron. The wave number k will be a complex number if $\omega < \omega_p$. Typical geomagnetic storm electromagnetic fields (GS-EMFs) are characterized by ultralow frequencies, hence the wavenumber k will be a complex number, namely, the ionosphere is a lossy medium for the EM wave. For $n = 10^3$ (1/cm^3) and $f = 30$ (mHz), the complex wavenumber $k = -j5.95 \times 10^{-3}$ (rad/m), which corresponds to the skin depth of $\delta = 169$ (m) [13]. For $n = 10^4$ (1/cm^3) and $f = 30$ (mHz), the complex wavenumber $k = -j1.88 \times 10^{-2}$ (rad/m), which corresponds to the skin depth of $\delta = 53$ (m). For $n = 10^5$ (1/cm^3) and $f = 30$ (mHz), the complex wavenumber

doi:10.6342/NTU202500706

$k = -j5.95 \times 10^{-2}$ (rad/m), which corresponds to the skin depth of $\delta = 16.9$ (m). The data of topography, sediment thickness and conductivity distribution in and around Japan are applied in the simulations [25], [26], [52], [53].

Fig.4.9 shows the current densities, extracted from the global MHD simulations. Fig.4.9(a) shows the current densities at geographic latitude of $40°N$. The magnitude of the current density during the May 2017 storm is about 0.15 (μA/m^2). The magnitude of the current density during the Halloween storm is about 0.3 (μA/m^2) at the dayside and 0.2 (μA/m^2) at the nightside. The current densities under the May 2017 storm and the Halloween storm manifest periodic features, with the period of about 30 (s). For the Carrington storm, the current density at the dayside reaches about 1 (μA/m^2) at $t \simeq 5$ (s), then oscillates between ± 0.5 (μA/m^2). The periodic features with the period of about 30 (s) is also observed. The current density at the nightside is about 0.5 (μA/m^2).

Fig.4.9(b) shows the distributions of J_y at $h \simeq 80$ (km) under different storms. The current density under the May 2017 storm manifest slight variations between $0 < \cos^{-1} z/r < 3\pi/2$. The magnitude increases to about 0.2 (μA/m^2) between $3\pi/2 < \cos^{-1} z/r < 2\pi$, corresponding to the north hemisphere at the dayside. The current density under the Halloween storm manifest a periodic like variation, with a magnitude of about 0.4 (μA/m^2). Under the Carrington storm, the magnitude of the current density is the largest, with the magnitude

doi:10.6342/NTU202500706

of about 0.6 (μA/m^2).

Fig.4.10 shows the distribution of electric field and magnetic field during the Halloween storm at the dayside at $z = 0$ and $t = 50$ (s) with $q = 500$. The selected time $t = 20$ (s) corresponds to the maximum magnitude of current density, as in Fig.4.9(a). Figs.4.10(a)-(c) show the distribution of electric fields. The magnitude of electric field on the ground is about 10 (mV/km). In general, the electric field on the ground is larger than that on the seawater, because the conductivity on the ground is smaller than that of the seawater. Strong electric field is observed along the coast lines because the charge accumulates around there, where large gradient of conductivity appears. The electric field is dominated by the horizontal components, E_x and E_y. The vertical component of electric field E_z manifests similar features, with stronger electric field along the coast lines, while its magnitude is smaller than those of E_x and E_y. Figs.4.10(d)-(f) show the distribution of magnetic field components. The magnitude of the magnetic field is about 300 (μA/m), and is dominated by the horizontal components, H_x and H_y. The magnetic field on the seawater is larger than that on the ground because the current induced by electromagnetic waves on the seawater is stronger than on the ground. The distribution of the vertical component of magnetic field H_z manifest similar feature to that of E_z, which is stronger along the coast line.

Fig.4.11 shows the distribution of electric field under May 2017 storm, Halloween storm

doi:10.6342/NTU202500706

and Carrington storm, respectively, at the dayside and nightside. The presented snapshots correspond to the maximum magnitudes, as in Fig.4.9(a). Fig.4.11(a) and (d) show that under the May 2017 storm, the magnitude of GIE at the dayside is about 3 (mV/km) around the coast lines, and about 1 order smaller at the inland region. For the nightside, the difference between coast line and inland becomes smaller, except the coast line at the northwest direction of Sea of Japan, as encircled by a red contour, implying the accumulations of charges.

Fig.4.11(b) and (e) show that under the Halloween storm, several coast line regions manifest large GIE, as encircled by red contours, with magnitude of about 15 (mV/km). The magnitude of GIE at inland region increases to about 2-3 (mV/km), which is comparable to the GIE along the coast line under May 2017 storm. The distributions at the dayside and nightside are similar, with smaller magnitude at the nightside.

Fig.4.11(c) and (f) show that under the Carrington storm, the magnitude of the GIE increases to about 20 (mV/km). The large GIE along the coast lines extends significantly. Some inland regions, which does not confront strong GIE under other storms, manifest strong GIE under the Carrington storm, as marked by the white contours. The distributions at the dayside and nightside are similar, with smaller magnitude at the nightside.

doi:10.6342/NTU202500706

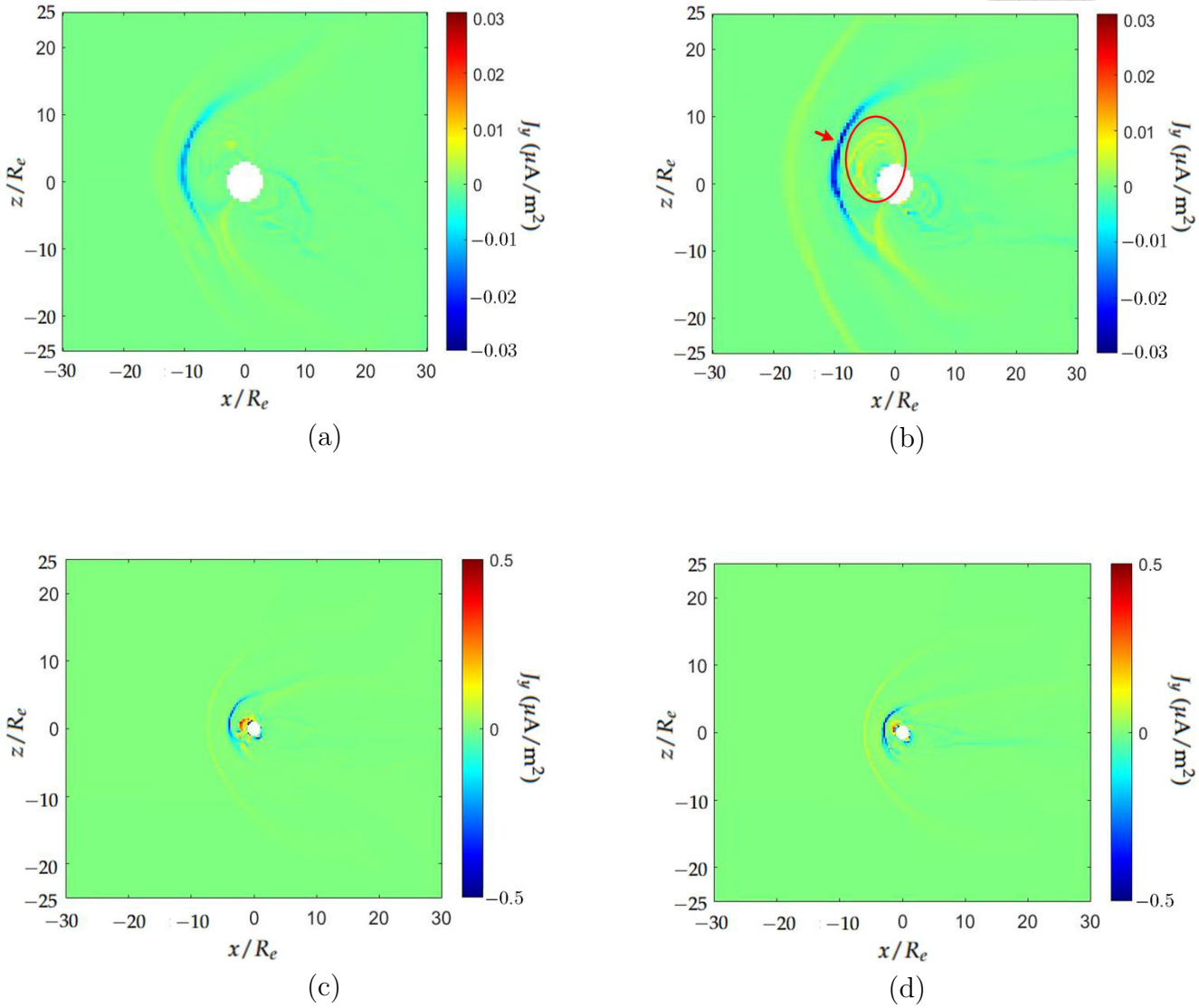

Figure 4.3: Comparison of current density distributions in magnetosphere under steady solar wind, 2017 storm, Halloween storm and Carrington storm, respectively, (a) steady solar wind, (b) May 2017 storm, (c) Halloween storm, (d) Carrington storm.

doi:10.6342/NTU202500706

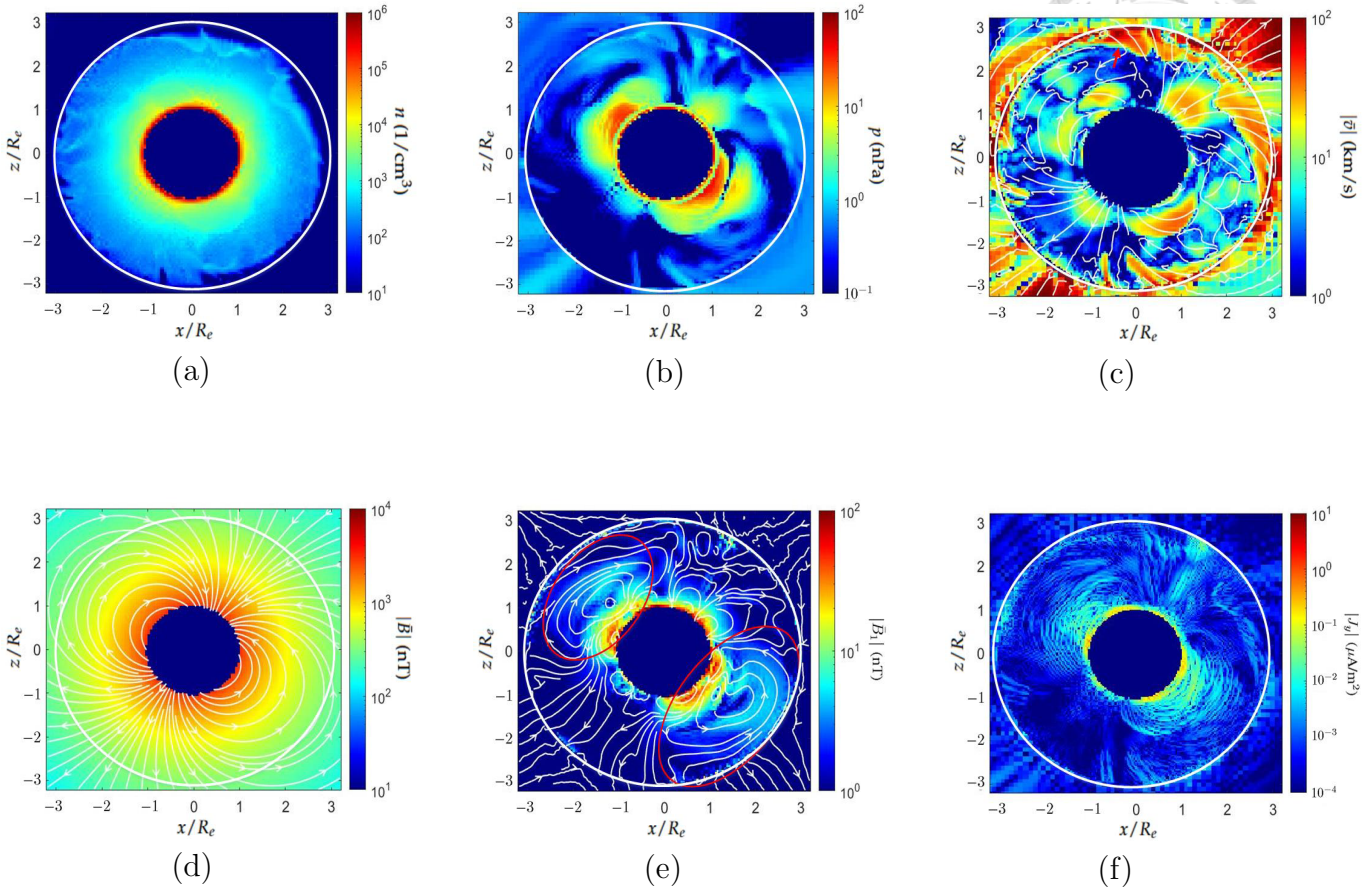

Figure 4.4: Distribution of plasma variables, magnetic field and current density, respectively, under steady solar wind within $3R_e$ at $t' = 80$ ($t = 75$ s), (a) n, (b) p, (c) $\bar{v}$, (d) $\bar{B}$, (e) $\bar{B}_1$, (f) J_y. The streamlines in (c) represents the direction of plasma flows, and those in (d) and (e) represents the magnetic field lines of $\bar{B}$ and $\bar{B}_1$, respectively. The white contours manifest the inner boundaries.

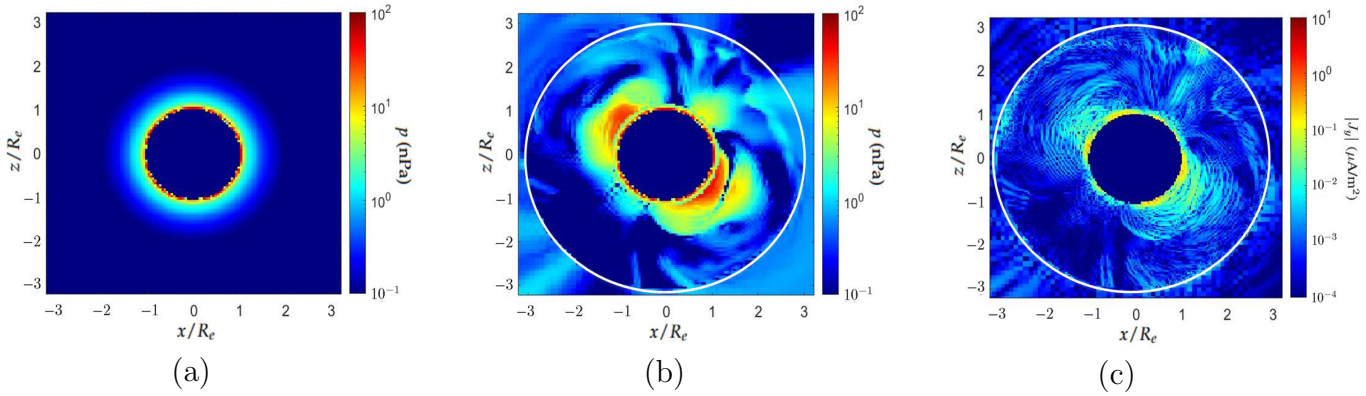

Figure 4.5: Distribution of gas pressure and current density under steady solar wind within $3R_e$, (a) p at $t = 0$, (b) p at $t' = 80$ ($t = 75$ s), (c) $|J_y|$ at $t' = 80$ ($t = 75$ s). The white contours manifest the inner boundaries.

doi:10.6342/NTU202500706

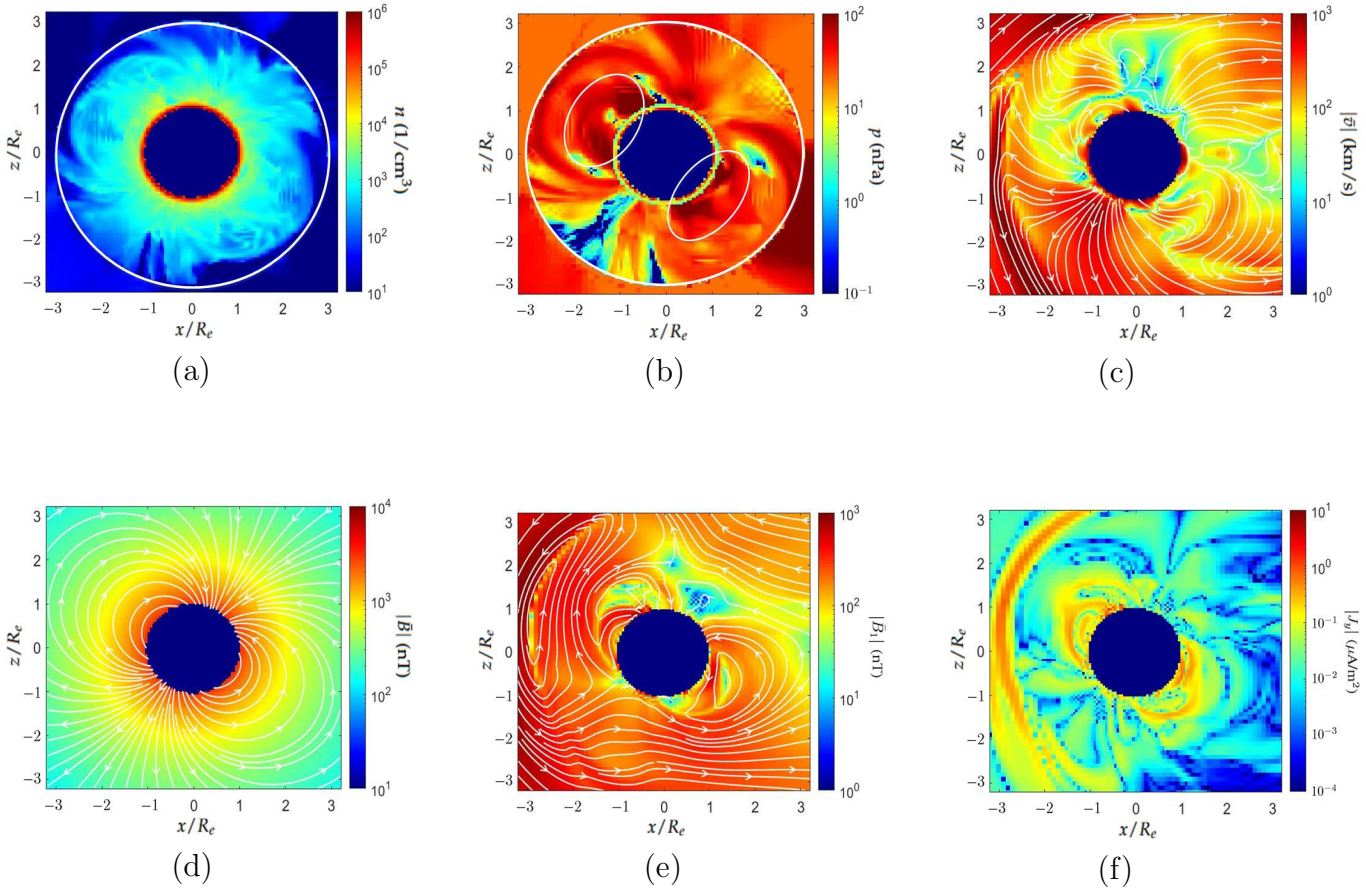

Figure 4.6: Distribution of plasma variables, magnetic field and current density, respectively, under Carrington storm around the Earth, (a) n, (b) p, (c) $\bar{v}$, (d) $\bar{B}$, (e) $\bar{B}_1$, (f) J_y. The streamlines in (c) represents the direction of plasma flows, and those in (d) and (e) represents the magnetic field lines of $\bar{B}$ and $\bar{B}_1$, respectively. The white contours manifest the inner boundaries.

doi:10.6342/NTU202500706

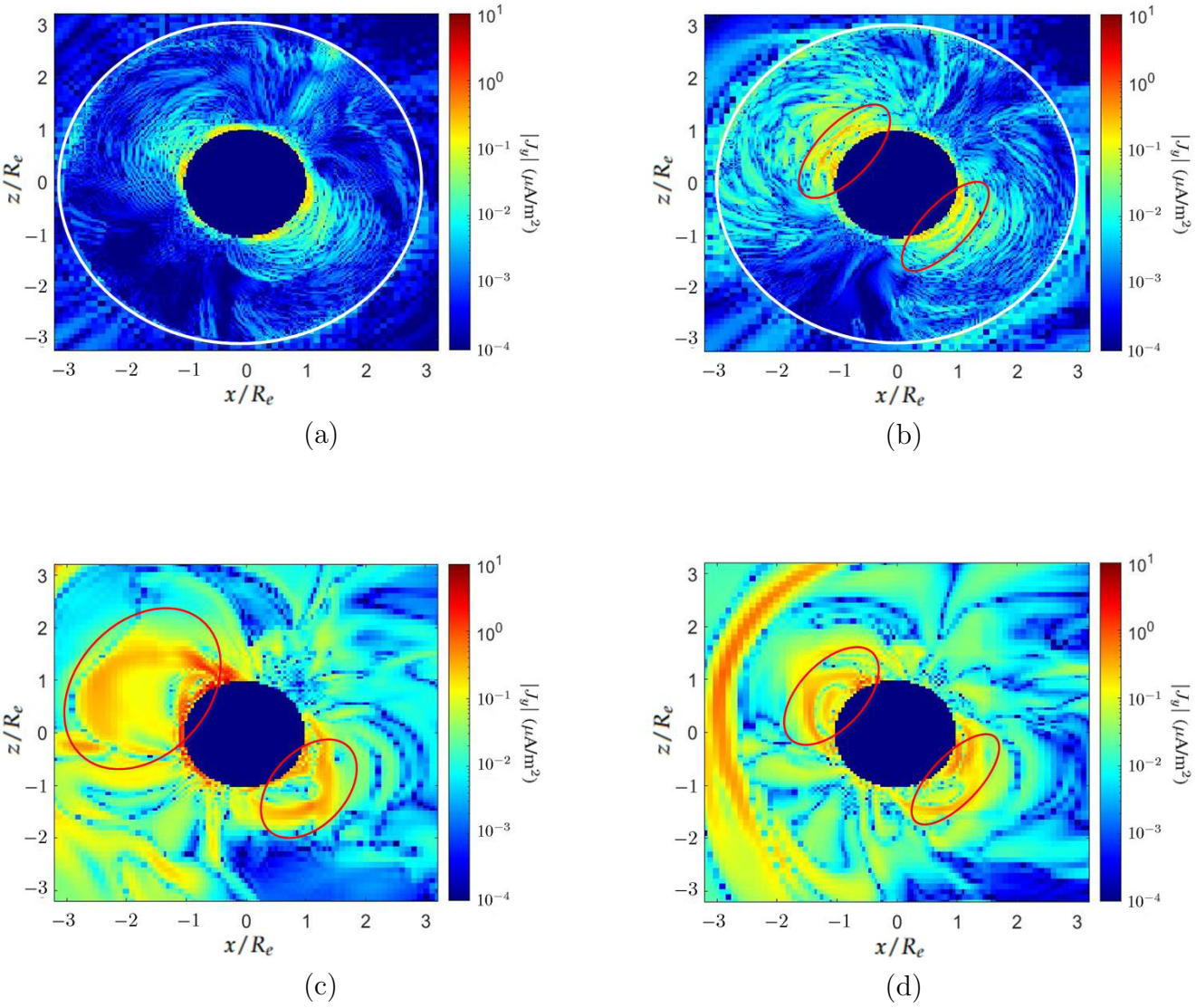

Figure 4.7: Comparison of current density distributions in ionosphere under steady solar wind, 2017 storm, Halloween storm and Carrington storm, respectively, (a) steady solar wind, (b) May 2017 storm, (c) Halloween storm, (d) Carrington storm. The white contours manifest the inner boundaries.

doi:10.6342/NTU202500706

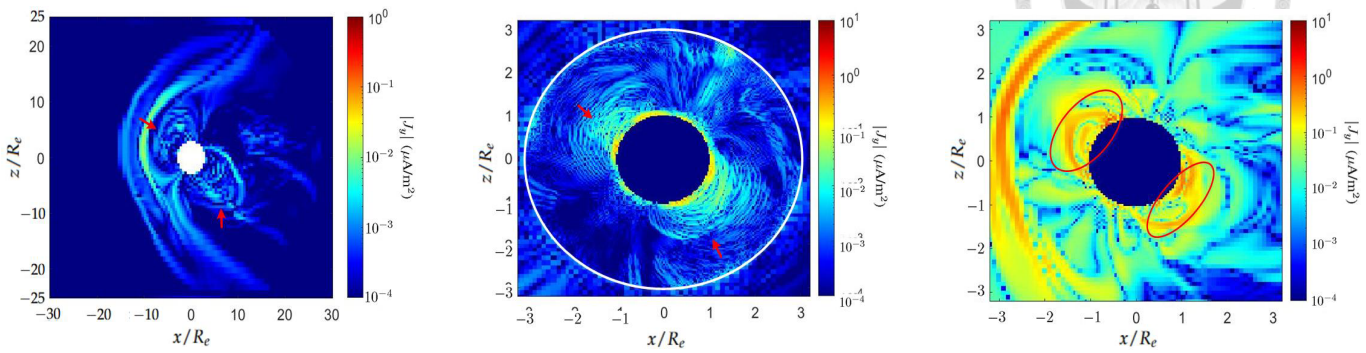

(a) (b) (c)

Figure 4.8: Distributions of current density in the magnetosphere and ionosphere under steady solar wind and Carrington storm, (a) magnetosphere under steady solar wind, (b) ionosphere under steady solar wind, (c) ionosphere under Carrington storm.

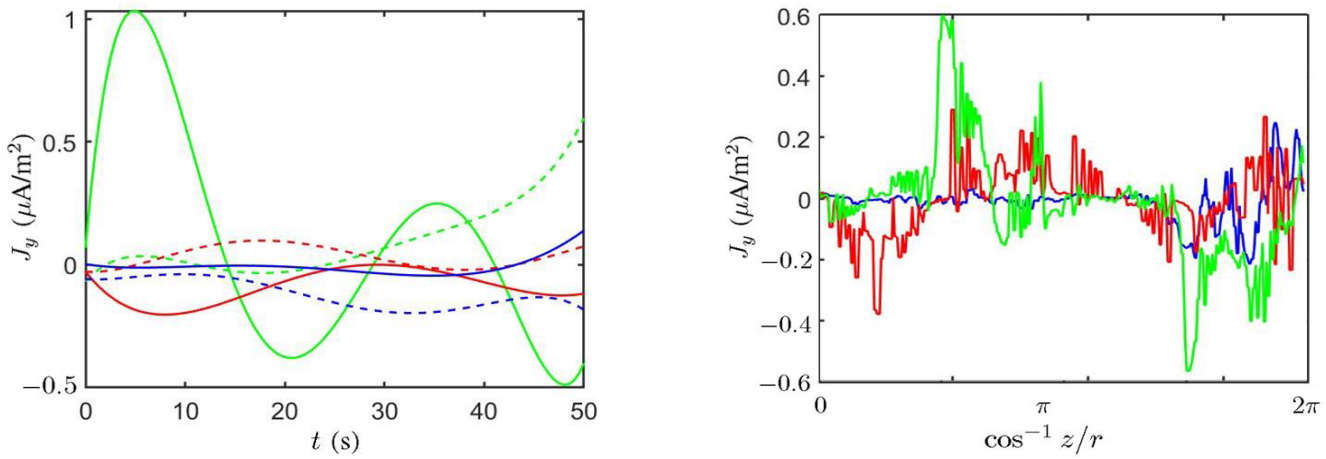

(a) (b)

Figure 4.9: Current densities extracted from the global MHD simulations; (a) current density at geographic latitude of $40°N$, solid line: dayside, dashed line: nightside, (b) distribution of J_y at $h \simeq 80$ (km). blue: May 2017 storm, red: Halloween storm, green: Carrington storm.

doi:10.6342/NTU202500706

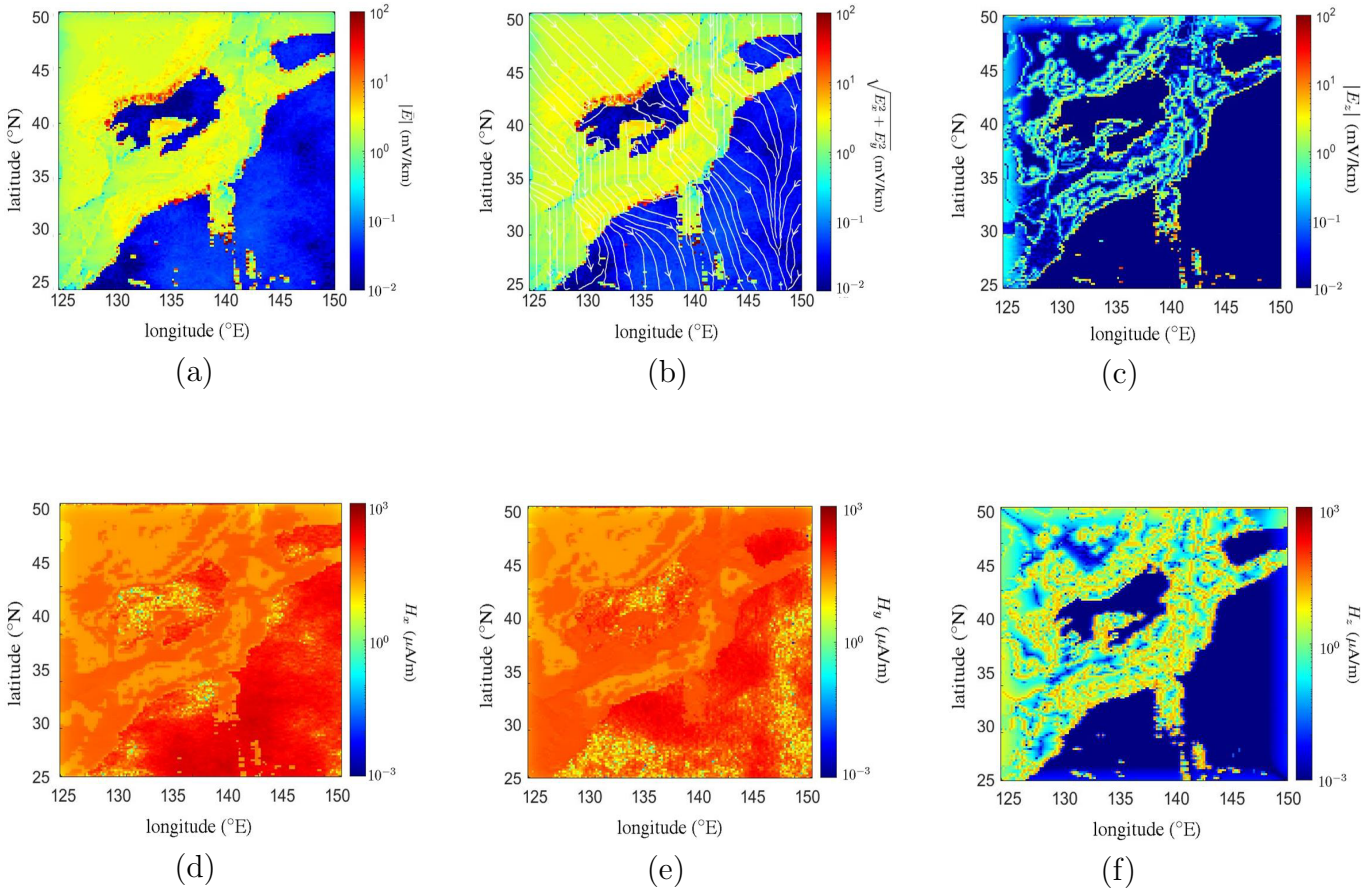

Figure 4.10: Distribution of electric field and magnetic field during Halloween storm at the dayside at $z = 0$ and $t = 50$ (s) with $q = 500$, (a) $|\bar{E}|$, (b) $\sqrt{E_x^2 + E_y^2}$, streamlines mark the direction of electric field lines, (c) E_z, (d) H_x, (e) H_y, (f) H_z.

doi:10.6342/NTU202500706

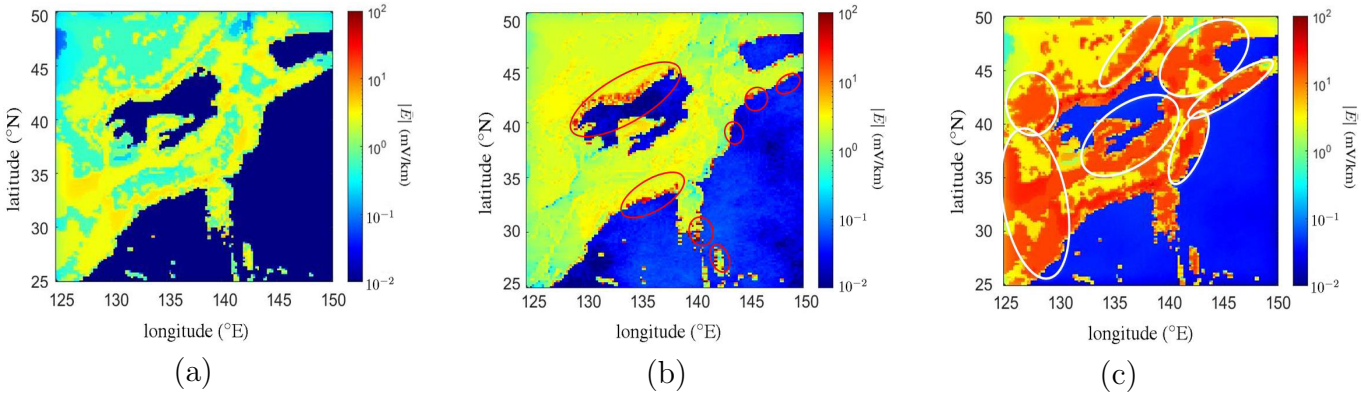

Figure 4.11: Distribution of electric field under May 2017 storm, Halloween storm and Carrington storm, respectively, at the dayside and nightside, (a) May 2017 storm at dayside, (b) Halloween storm at dayside, (c) Carrington storm at dayside, (d) May 2017 storm at nightside, (e) Halloween storm at nightside, (f) Carrington storm at nightside. The presented snapshots correspond to the maximum magnitudes, as in Fig.4.9(a).

doi:10.6342/NTU202500706

Chapter 5

Conclusions

The GIEs, under May 2017 storm, Halloween storm and Carrington storm, at the dayside and nightside, respectively, have been simulated. The magnetospheric and ionospheric responses are simulated by using the global MHD model. Then, the GIE are simulated, with the current sources obtained from the global MHD simulations. The GIEs under three solar storms are quantitatively estimated to evaluate possible hazards of solar storms. Phenomena akin to the Van Allen radiation belts are revealed in the simulations. In the magnetosphere, the bow shock is highly compressed towards the Earth, with extremely high particle number density, and the current density is enhanced around the Earth when the solar storms arrives at the Earth. In the ionosphere, the perturbation of magnetic field is much smaller than the geomagnetic field. Under the Halloween and Carrington storms, the current density flowing in the ionosphere is significantly enhanced because the magnetopause is highly compressed and the strong solar wind directly affects the plasma at the vicinity of the Earth. On the

doi:10.6342/NTU202500706

Earth's surface, the magnitude of GIE at the dayside is about 3 (mV/km) around the coast lines, and about 1 order smaller at the inland region under the May 2017 storm. Large GIE is induced at the northwest direction of Sea of Japan. Under the Halloween storm, several coast line regions manifest large GIE with magnitude of about 10 (mV/km). The magnitude of GIE at inland region is also increased to about 2-3 (mV/km). Under the Carrington storm, the magnitude of the GIE increases to about 20 (mV/km). Some inland regions, which does not confront strong GIE under other storms, manifest strong GIE under the Carrington storm.

doi:10.6342/NTU202500706

Bibliography

[1] N. Buzulukova and B. Tsurutani, "Space weather: from solar origins to risks and hazards evolving in time," *Frontiers in Astronomy and Space Science*, vol. 9, DOI 10.3389, fspas.2022.1017103, December, 2022.

[2] J. Zheng, J. Huang, Z. Li, W. Li, Y. Han *et al.*, "Multiple-band electric field response to the Geomagnetic Storm on 4 November 2021," *Remote Sensing*, vol. 16, iss. 18, no. 3497, 2024.

[3] N. A. Frissell, J. S. Vega, E. Markowitz *et al.*, "High-frequency communications response to solar activity in September 2017 as observed by amateur radio networks," *Space Weather*, vol. 17, issue 1, pp. 118-132, 2019.

[4] P. V. S. Rama Rao, S. Gopi Krishna, J. Vara Prasad *et al.*, "Geomagnetic storm effects on GPS based navigation," *Annales Geophysicae*, vol. 27, pp. 2101-2110, 2009.

[5] X. Luo, J. Du, Y. Lou *et al.*, "A method to mitigate the effects of strong geomagnetic storm on GNSS precise point positioning," *Space Weather*, vol. 20, issue 1, 2022.

doi:10.6342/NTU202500706

[6] T. Dang, X. Li, B. Luo *et al.*, "Unveiling the space weather during the Starlink satellites destruction event on 4 February 2022," *Space Weather*, vol. 20, issue 8, 2022.

[7] S. Bruinsma, T. D. de Wit, T. Fuller-Rowell *et al.*, "Thermosphere and satellite drag," *Advances in Space Research*, accepted, 2023.

[8] A. Keiling, O. Marghitu and M. Wheatland, *Electric Currents in Geospace and Beyond*, John Wiley & Sons, Inc., Hoboken, USA, 2018.

[9] M. Kellinsalmi, A. Viljanen, L. Juusola and S. Kaki, "The time derivative of the geomagnetic field has a short memory," *Annales Geophysicae*, vol. 40, pp. 545-562, 2022.

[10] J. G. Kappenman and V. D. Albertson, "Bracing for the geomagnetic storms," *IEEE Spectrum*, vol. 27, pp. 27-33, 1990.

[11] T. S. Molinski, "Why utilities respect geomagnetically induced currents," *Journal of Atmospheric and Solar-Terrestrial Physics*, vol. 64, pp. 1765-1778, 2002.

[12] B. Adhikari, N. Sapkota, S. Dahal *et al.*, "Spectral characteristic of geomagnetically induced current during geomagnetic storms by wavelet techniques," *Journal of Atmospheric and Solar-Terrestrial Physics*, vol. 192, 104777, 2019.

[13] D. K. Cheng, *Field and Wave Electromagnetics*, 2nd edition, Addison-Wesley Publishing Company, 1983.

doi:10.6342/NTU202500706

[14] N. A. Krall and A. W. Trivelpiece, *Principles of Plasma Physics*, McGraw-Hill Book Company, 1973.

[15] A. Pulkkinen, M. Kuznetsova, A. Ridley *et al.*, "Geospace environment modeling 2008-2009 challenge: ground magnetic field perturbations," *Space Weather*, vol. 9, S02004, 2011.

[16] N. K. Kwagala, M. Hesse, T. Moretto *et al.*, "Validating the space weather modeling framework (SWMF) for applications in northern Europe," *Journal of Space Weather and Space Climate*, vol. 10, no. 33, 2020.

[17] J. Wang, A. Du, Y. Zhang *et al.*, "Modeling the Earth's magnetosphere under the influence of solar wind with due northward IMF by the AMR-CESE-MHD model," *Science China Earth Sciences*, vol. 58, pp. 1235-1242, 2015.

[18] C.-M. Lai and J.-F. Kiang, "Comparative study on planetary magnetosphere in the solar system," *Sensors*, vol. 20, issue 6, no. 1673, 2020.

[19] M. L. Goodman, "A three-dimensional, iterative mapping procedure for the implementation of an ionosphere-magnetosphere anisotropic Ohm's law boundary condition in global magnetohydrodynamic simulations," *Annales Geophysicae*, vol. 13, pp. 843-853, 1995.

doi:10.6342/NTU202500706

[20] A. J. Ridley Y. Deng and G. Toth, "The global ionosphere-thermosphere model," *Journal of Atmospheric and Solar-Terrestrial Physics*, vol. 68, pp. 839-864, 2006.

[21] D. Bilitza, M. Pezzopane, V. Truhlik *et al.*, "The international reference ionosphere model: a review and description of an ionospheric benchmark," *Reviews of Geophysics*, vol. 60, e2022RG000792, 2022.

[22] B. Nava, P. Coisson and S. M. Radicella, "A new version of the NeQuick ionosphere electron density model," *Journal of Atmospheric and Solar-Terrestrial Physics*, vol. 70, pp. 1856-1862, 2008.

[23] R. E. Daniell, L. D. Brown, D. N. Anderson *et al.*, "Parameterized ionospheric model: a global ionospheric parameterization based on first principles models," *Radio Science*, vol. 30, no. 5, pp. 1499-1510, 1995.

[24] Y. Deng, C. Sheng, B. T. Tsurutani *et al.*, "Possible influence of extreme magnetic storms on the thermosphere in the high latitudes," *Space Weather*, vol. 16, pp. 802-813, 2018.

[25] S. Fujita, I. Fujii, A. Endo and H. Tominaga, "Numerical modeling of spatial profiles of geomagnetically induced electric field intensity in and around Japan," *Technical Report of the Kakioka Magnetic Observatory*, vol. 14, no. 2, pp. 35-50, 2018.

doi:10.6342/NTU202500706

[26] S. Nakamura, Y. Ebihara, S. Fujita *et al.*, "Time domain simulation of geomagnetically induced current (GIC) flowing in 500-kV power grid in Japan including a three-dimensional ground inhomogeneity," *Space Weather*, vol. 16, iss. 12, pp. 1946-1959, 2018.

[27] M. Lehtinen and R. J. Pirjola, "Currents produced in earthed conductor networks by geomagnetically-induced electric fields," *Annales Geophysicae*, vol. 3, no. 4, pp. 479-484, 1985.

[28] R. J. Pirjola, D. H. Boteler, L. Tuck and S. Marsal, "The Lehtinen-Pirjola method modified for efficient modelling of geomagnetically induced currents in multiple voltage levels of a power network," *Annales Geophysicae*, vol. 40, pp. 205-215, 2022.

[29] D. Oyedokun, M. Heyns, P. Cilliers and CT Gaunt, "Frequency components of geomagnetically induced currents for power system modelling," *2020 International SAUPEC/RobMech/PRASA Conference*, Cape Town, South Africa, pp. 1-6, 2020.

[30] A. L. Fleetham, S. E. Milan, S. M. Imber *et al.*, "The relationship between large dB/dt and field-aligned currents during five geomagnetic storms," *Journal of Geophysical Research: Space Physics*, vol. 129, e2024JA032483, 2024.

doi:10.6342/NTU202500706

[31] C.-J. Chang and J.-F. Kiang, "Simulations of switchback, fragmentation and sunspot pair in δ-sunspots during magnetic flux emergence," *Sensors*, vol. 21, Iss. 2, no. 586, 2021.

[32] P. Stubbe and T. Hagfors, "The earth's ionosphere: a wall-less plasma laboratory," *Surveys in Geophysics*, vol. 18, pp. 57-127, 1997.

[33] J. Raeder, "Global magnetohydrodynamics - a tutorial," *Space Plasma Simulation. Lecture Notes in Physics*, vol. 615, Springer, Berlin, Heidelberg, 2003.

[34] E. F. Toro, *Riemann solvers and numerical methods for fluid dynamics: A Practical introduction*, Third Edition, 2009.

[35] P. Londrillo and L. D. Zanna, "On the divergence-free condition in Godunov-type schemes for ideal magnetohydrodynamics: the upwind constrained transport method," *Journal of Computational Physics*, vol. 195, pp. 17-48, 2004.

[36] Tatsuki Ogino, "A three-dimensional MHD simulation of the interaction of the solar wind with the Earth's magnetosphere: the generation of field-aligned currents," *Journal of Geophysical Research*, vol. 91, no. A6, June 1, 1986.

[37] M. Walt, *Introduction to Geomagnetically Trapped Radiation*, Cambridge University Press, 1994.

doi:10.6342/NTU202500706

[38] D. E. Winch, D. J. Ivers, J. P. R. Turner *et al.*, "Geomagnetism and Schmidt quasi-normalization," *Geophysical Journal International*, vol. 160, pp. 487-504, 2005.

[39] H. Zhou, L. Turc, Y. Pfau-Kempf *et al.*, "Magnetospheric responses to solar wind Pc5 density fluctuations: results from 2D hybrid Vlasov simulation," *Frontiers in Astronomy and Space Sciences*, 9:984918, September 02, 2022.

[40] V. B. Ovodenko, I. Zakharenkova, M. V. Klimenko *et al.*, "Ionospheric irregularities over Norilsk during the 27-28 May 2017 geomagnetic storm," *2nd URSI AT-RASC, Gran Canaria*, 2018.

[41] Y. A. Tariku, "The geomagnetic storm time response of the mid latitude ionosphere during solar cycle 24," *Radio Science*, vol. 56, e2021RS007340, 2021.

[42] B. T. Tsurutani, A. J. Mannucci, B. Iijima *et al.*, "The extreme Halloween 2003 solar flares, ICMEs, and resultant extreme ionospheric effects: a review," *Advances in Space Research*, vol. 37, pp. 1583-1588, 2006.

[43] G. Siscoe, N. U. Crooker and C. R. Clauer, "Dst of the Carrington storm of 1859," *Advances in Space Research*, vol. 38, pp. 173-179, 2006.

doi:10.6342/NTU202500706

[44] H. Hayakawa, S. Bechet, F. Clette *et al.*, "Magnitude estimates for the Carrington flare in 1859 September: as seen from the original records," *Astrophys. J.*, vol. 954:L3 (10pp), September 1, 2023.

[45] E. W. Cliver, C. J. Schrijver, K. Shibata and I. G. Usoskin, "Extreme solar events," *Living Reviews in Solar Physics*, vol. 19, no. 2, 2022.

[46] X. Li, M. Temerin, B. T. Tsurutani and S. Alex, "Modeling of 1-2 September 1859 super magnetic storm," *Advances in Space Research*, vol. 38, pp. 273-279, 2006.

[47] H. Zamani, K. Sheshyekani and P. Dehkhoda, "3-D FDTD method for fast calculation of geomagnetic storm electromagnetic fields," *IEEE Transactions on Electromagnetic Compatibility*, vol. 63, no. 4, August 2021.

[48] R. M. Shore, K. A. Whaler, S. Macmillan *et al.*, "Ionospheric midlatitude electric current density inferred from multiple magnetic satellites," *Journal of Geophysical Research: Space Physics*, vol. 118, pp. 5813-5829, 2013.

[49] A. Z. Elsherbeni and V. Demir, *The finite-difference time-domain method for electromagneitcs with MATLAB simulations*, 2nd edition, 2015.

[50] J.-P. Berrut and L. N. Trefethen, "Barycentric Lagrange Interpolation," *SIAM Review*, vol. 46, no. 3, pp. 501-517, 2004.

doi:10.6342/NTU202500706

[51] Y. Zhang and J. J. Simpson, "Extrapolation within the Time-Stepping Loop of FDTD Models," *IEEE Transactions on Antennas and Propagation*, vol. 72, no. 4, April 2024.

[52] NOAA National Geophysical Data Center, *ETOPO1 1 Arc-Minute Global Relief Model. NOAA National Centers for Environmental Information*, 2009.

[53] G. Laske and T. G. Masters, "A global digital map of sediment thickness," *EOS Transactions American Geophysical Union*, 78(46), 483.

[54] W. Li and M. K. Hudson, "Earth's Van Allen radiation belts: from discovery to the Van Allen Probes eras," *Journal of Geophysical Research: Space Physics*, vol. 124, pp. 8319-8351, 2019.

[55] https://web.archive.org/web/20200306135737/https://www.nasa.gov/content/goddard/van-allen-probes-spot-impenetrable-barrier-in-space.

[56] C.-J. Chang and J.-F. Kiang, "Simulations on synchrotron radiation intensity and rotation measure of relativistic magnetized jet PKS 1502+106," *Universe*, vol. 9, no. 235, 2023

[57] C.-J. Chang and J.-F. Kiang, "Reconstruction of Fermi and eROSITA bubbles from magnetized jet eruption with simulations," *Universe*, vol. 10, no. 279, 2024.

doi:10.6342/NTU202500706